GPS Measurements of Present day crustal deformation within the Lebanese Restraining Bend

along the Dead Sea Transform

_____

A Thesis

Presented to

the Faculty of the Graduate School

at the University of Missouri-Columbia

_____

In Partial Fulfillment

of the Requirements for the Degree

Master of Science

_____

by

RANI JAAFAR

Dr. Francisco Gomez, Thesis Supervisor

DECEMBER 2008

The undersigned, appointed by the dean of the Graduate School, have examined the thesis entitled:

GPS Measurements of Present day crustal deformation within the

Lebanese Restraining Bend along the Dead Sea Transform

Presented by Rani Jaafar

A candidate for the degree of Master of Science

And hereby certify that in their opinion it is worthy of acceptance.

_____

Dr. Francisco Gomez

_____

Dr. Robert Bauer

_____

Dr. Brent Rosenblad

Acknowledgements

Table of Contents

List of Figures

List of Tables

GPS Measurements of Present day crustal deformation within the

Lebanese Restraining Bend along the Dead Sea Transform

Rani Jaafar

Dr. Francisco Gomez, Thesis Supervisor

ABSTRACT

The Lebanese restraining bend is a 200 km long bend with a left lateral sense of slip located along the Dead Sea fault system (DSFS) between 33.2 and 34.6 degrees north latitude. The DSFS is a transform plate boundary fault system accommodating the differential northward movement of Arabian and Sinai plates relative to the Eurasian plate. Within the Lebanese Restraining bend, The DSFS splays into five left-lateral strike-slip faults, forming a positive flower structure. This study combines GPS measurements from Lebanon, where surveys span about 5.5 years, with sites from the Anti Lebanon Mountains in SW Syria for a more complete view of crustal deformation in the restraining bend. The GPS network includes continuous GPS sites and 27 campaign sites: 14 sites in Lebanon installed in 2002, 8 sites in Lebanon installed in 2005, and 5 sites in southwestern Syria. Preliminary velocities for older campaign sites have uncertainties less than 0.75 mm/yr, whereas newer sites have around 1.5 mm/yr uncertainties. The improved spatial coverage and reduced uncertainties allow constructing; 1) elastic fault models that explore strain partitioning between two strike slip faults (Yammouneh and Serghaya faults) and a generalized off-shore thrust fault to accommodate convergence in the restraining

bend, and 2) continuum (velocity gradient) models that explore infinitesimal strain and rotation rates. The models suggest a displacement rate of 4.5-5.5 mm/yr along the Yammouneh fault and a counter clock wise rotation of 0.5^{o}-1.75^{o}/MA within the bend. This study provides an essential tool for assessing the seismic hazard in the vicinity of the Lebanese restraining bend.

Chapter 1

Active tectonics and seismology of the LRB

Introduction:

The Dead Sea Transform is a major plate tectonic feature in the Eastern Mediterranean region with a historical record of large devastating earthquakes. The Dead Sea Transform forms the boundary between the Sinai plate (African plate) to the west and the Arabian plate to the east, and it extends nearly 1000 km, linking sear-floor spreading in the Red Sea to the collision of the Arabian and Eurasian plates (Figure 1.1). This transform system undergoes left-lateral slip as a result of the differential northward movement of the Arabian and African plates relative to the Eurasian plate. The Dead Sea Transform is divided into two major sections, a northern and a southern section, that are connected by a right step restraining bend that lies within present day Lebanon and is referred herein as the Lebanese restraining bend (LRB). The Lebanese restraining bend spans 180 km, striking NNE-SSW between latitudes 33.2^o N and 34.6^o N. The LRB includes two mountain chains; the Mount Lebanon to the west of the bend and the Anti-Lebanon to the east of the bend, with the Bekaa valley in between (figure 1.1). Figure 1.11 shows the existing structural similarities between the LRB and the San Andreas fault in California.

Why study the Lebanese Restraining Bend (LRB)? To begin, The LRB is still poorly understood and fault kinematics within the bend are being debated in recent publications. According to Butler et al. (1998), RF has been the main active strand of the DST for the past 6 Ma, while according to others, YF is the main Lebanese component of the DST (Dubertret, 1947, 1970; Hancock & Atiya, 1979; Gomez et al. 2006). Moreover, it is an analog to other major faults such as the San Andreas fault (Figure 1.11). In other words, implications of this study could be used to further understand other major faults.

Furthermore, The LRB is a history of recorded devastating earthquakes that date back to 1365 BC (Table 1.1). Recorded earthquakes are essential in the study of faults and are available in limited regions around the world. Results and fault kinematics obtained in this project would be used in seismic hazard assessment and evaluating threat to mega-cities located within the vicinity of the LRB.

Structural Elements of the LRB:

Within the LRB the relatively simple structure of the DST branches into several prominent structures across a 100 km wide zone.

Faults:

At the 33.2^o latitude (South of the Beqaa Valley) the Dead Sea transform (DST) splays into one continuous fault and four other discontinuous faults creating a positive flower structure and causing uplift in the southern part of the LRB. The continuous fault is the Yammouneh fault while the discontinuous ones are the Serghaya fault, Rachaya fault, Hasbaya fault, and Roum fault (figure 1.4 & 1.5) (Nemer, 2005). The Yammouneh fault (YF) is defined as a 170 km left lateral that displays a horizontal and a vertical slip (Dubertret, 1955; Heismann and Ron, 1987; Daeron et al., 2004). It is also believed by many researchers that the Yammouneh fault is the main Lebanese component of the Dead Sea transform (Dubertret, 1947, 1970; Hancock & Atiya, 1979). The Serghaya fault (SF) displays a sinistral sense of slip and is the second major fault with respect to its slip rate in the LRB. It accounts for 25 % of the total predicted motion between the Arabian plate and the African plate (Sinai) (Gomez et al., 2003). The Rachaya fault (RcF) is around 45 km long. It also exhibits a sinistral sense of slip (Heimann et al. 1990) and it forms with the Serghaya fault a harmonized fault system around the Mount Lebanon block (Gomez

et al., 2003). The Hasbaya (HF) fault extends for around 50 km. The HF was mapped as a discontinuous fault with minor throw and localized basaltic covers (Dubertret, 1940, 1951; Butler et al. 1998). The Roum (RF) fault is the westernmost branch of the positive flower structure within the LRB, and the only fault that has a N-S trend like the southern section of the DST (figure 1.4). The RF extends for around 40 km and exhibits a sinistral and a vertical sense of slip (Nemer, 2005).

In addition to these discussed major faults, other minor faults are spatially related to the primary faults in Lebanon. In Mount Lebanon there are several right lateral E-W striking faults spanning between the northern and the southern part of the LRB. It is believed by Ron (1987, 1990) that these blocks reflect a bookshelf faulting accommodating the regional sinistral sense of slip of the Dead Sea transform. Other minor faults of similar orientation, sense of slip, and resulting from block rotation are localized on the eastern side of the LRB (figure 1.6) (Ron, 1987, 1990). Furthermore, thrust faults are a major geological structure within a restraining bend, and they are the resultant of the transpression zone. From some geological and offshore earthquake epicenters, like the 551 Beirut-Tripoli event (table 1.1), we can deduce that sub-parallel thrust faults exist within the vicinity of the transpression zone (figure 1.4). Recently, submarine ruptures and scarps, that cut the smoothly sediment-mantled seafloor, were discovered by the SAR deep towed acoustic system project. The discovered scarps establish the existence of a 160 km offshore thrust belt, and this thrust fault is most likely the source of the 551 earthquake (Elias et al., 2007)

Folds:

The LRB involves a structural framework composed of two anticlinorium and a synclinorium. The NNE-SSW trending Mount Lebanon to the west and Anti Lebanon to the east represent the two anticlinoria, and the Beqaa Valley between them represents the synclinorium (figure 1.4 and 1.7B). The anticlinoriua and the synclinorium are superimposed by a series of minor folds (Figure 1.5) (Walley 1988, 1998). This structural arrangement is considered to be a direct demonstration of the transpressional zone resulting from the right step in sinistral DST (Hancock & Atiya, 1979). Mount Lebanon is marked by the presence of an anticline forming the Niha-Barouk range whose hinge trends parallel to the Yammouneh fault. A large monocline runs from the western edge of the Chouf up to the latitude of Tripoli inland of the coast, and part of this feature contains steeply dipping rock strata (figure 1.10). Folds of a smaller scale exist around the south-western part of the Niha-Barouk range such as the overturned beds at Nabi Ayoub. Other small folds are visible within Mount Lebanon, such as the Jebel Terbol fold which is located North of Tripoli (Figure 1.9) (Walley, 1998). The oblique fold belt found in NW Lebanon next to Tripoli is believed to be detached from deep-seated crustal transform faults (Butler et al., 1998). Other small NE-SW trending anticlines are found in the Bekaa valley synclinorium, and are located just to the east of the Yammouneh fault (Figure 1.5) (Walley, 1998). On the other hand, folding in Anti Lebanon is expressed in Mount Hermon as a broad anticline that outcrops its Jurassic core. The Anti Lebanon anticlinoria is superposed to the west by a regional syncline abuts diagonally the southern part of the Yammouneh fault (Nemer, 2005).

Seismicity:

The earthquake activity of the Lebanese restraining bend has been assessed in several publications using historical and instrumental records, as well as Paleoseismic studies.

Historical and Instrumental records:

The eastern Mediterranean has witnessed many civilizations in the past 3500 years, such as: the Phoenicians from 1200 to 800 B.C, the Greeks, the Egyptians (pharaohs), the Romans from 50 BC to 400 A.C, the Hebrews, the Byzantium from 400 A.C to 1453 AC, and others. These different civilizations provide us with valuable records of earthquakes that took place along the Dead Sea Transform fault. The more recent earthquake information was collected from diaries and letters written by merchants, clerics, and church officials such as correspondence of the Jewish communities in the region (Ambraseys & Barazangi, 1989). The first recorded earthquake dates back to 1365 BC (Sbeinati et al., 2005). This provides us with more than 3350 years of strong earthquake data. The following table contains the major earthquakes that took place around the Lebanese restraining bend in the past 3300 years (table 1.1).

The instrumental recorded seismicity of the LRB indicates that the transpression zone is still active (figure 1.2). The major instrumentally recorded earthquakes are as follow: The Ms 4.8 and 5.1double shocks of 16 March 1956, the Ms 5.6 and 5.0 double shocks of 26 March 1997 (International Seismological center). Note that the seismicity of the LRB has been rather quiet in the last 100 years compared to historical data (e.g., Sbeinati et al., 2005; Ambraseys & Jackson 1998)

Paleoseismic:

Paleoseismic studies carried out on major Lebanese faults uncovered the recurrence rates and date of the last seismic events for each of these faults. The YF has a return

Date	Main Affected Places	Estimated Magnitude	Epicentral Area	Associated effects/remarks
~1365 BC	Ugarit	-	Ugarit (Syria)	Tsunami, fire
590 BC	Tyre	Ml 6.8	-	Tsunami in Lebanon
525 BC	Tyre, Sidon	Ml 7.5	-	Destruction in Tyre, Sidon, Bisri
19 AD	Sidon, Palestine, Syria	Ml 6.8	Hula basin	Destruction in Sidon
303-304 AD	Sidon, Tyre, Syria, Jerusalem	Ml 7.1, Ms 7.1	33.8 N, 34.3 E	Tsunami
341	Beirut	Ml 7.0	-	Aftershocks
348-349	Beirut/Arwad	Ml 7.0	-	-
502 Aug 22	Acre, Tyre, Sidon, Beirut, Palestine	Ml 7.0, Ms 7.2	33.0 N, 34.8 E	Acre destroyed
525 May	Beirut, Byblos Sidon	Ml 6.7	Off-shore Sidon	Aftershocks
551 Jul 9	Off-shore Lebanon	Ms 7.2	34.0 N, 35.5 E	Coastal uplift.
847 Nov 24	Damascus	Ml 6.2, Ms 7.5	34.4 N, 36.3E (Yammouneh fault)	Destruction in Damascus and homes
991 Apr 5	Baalbeck, Damascus	Ml 6.5, Ms 7.1	33.7 N, 36.4 E	Landslides, Aftershocks
1063 July 30 – Aug 27	Tripoli, Acre, Tyre	Ml 7.1, Ms 6.9	34.4N 36.2 E (Yammouneh Fault)	-
1202 May 20	Mont Lebanon, Baalbeck, Tyre, Damascus, Acre, Beirut …	Ms 7.5	33.7N 35.9 E	Tsunami, landslide, Aftershocks.
1705 Nov 24	Damascus, Tripoli	Ms 6.9	33.7 N, 36.6 E	Aftershocks
1759 Oct 30	Beirut, Aleppo, Damascus, Acre, Sidon, Jerusalem…	Ms 6.6	33.1 N, 35.6 E	Landslides west of Damascus, tsunami in Acre and Tripoli, aftershocks.
1759 Nov 25	Baalbeck, Serghaya, Damascus, Beirut, Sidon, Tripoli, Acre…	Ms 7.4	33.7 N, 36.1 E (Rachaya fault)	Landslides, Liquefaction.
1802	Baalbeck, Palestine	Ml 6.2	34.0 N, 36.2 E (Serghaya Fault)	-
1837 Jan 1	Safad, Nablus, Beirut, Damascus.	Ml 6.4, Ms 7.1	33.0 N 35.5 E (Roum Fault)	Tsunami in the Tiberias Lake
1873 Feb 14	Tyre, Beirut, Jerusalem, Acre	Ml 6.2	Off-shore Tyre	-

Table 1.1: Earthquake data from Nemer (2005), Ambraseys & Barazangi (1989), Gomez

et al. (2003), and Sbeinati et al. (2005).

period of ~1000-1100 yr with a last major earthquake dating back to May 20, 1202 (Nemer et al. 2008). SF revealed a return period of ~ 1300 years with the Nov 25, 1759 earthquake being its last (Gomez et al. 2003). Moreover, RF has witnessed a minimum of four faulting episodes in the last ~ 10,000 years with the Jan 1, 1837 earthquake being the last (Nemer and Meghraoui 2006). Finally, the offshore thrust belt has a return period of 1500-1750 yr with the Jul 9, 551 being its last major event (Elias et al. 2007 and Morhange et al. 2006).

Kinematics of the LRB:

   Prior constraints on the kinematics of the LRB are summarized below.

Slip rates:

   Slip rates were discussed and published by several researchers and were mainly based on geologic slip rates and elastic slip rate models. To begin, the geologic slip rates were based on paleoseismological and geomorphological studies. The geomorphologic, which consists of the study of the evolution of landforms, suggested a slip rate of 5.1 ± 1.3 mm/yr (Daeron et al., 2004) and 5.0 ± 1.1 mm/yr (Gomez et al., 2007) for the Yammouneh fault. Gomez et al., (2003) suggested a slip rate of 1.4 ± 0.2 mm/yr along the Serghaya fault which only accounts for 25 % of the total predicted motion of the Arabian plate relative to the African plate along the Lebanese Restraining Bend. He also suggested that the Yammouneh fault accommodates most of the expected strike slip motion, which has a calculated rate of ≈ 4.1 mm/yr. According to most investigators, the Yammouneh fault is the main Lebanese strand of the Dead Sea transform (Dubertret, 1947, 1970; Hancock and Atiya 1979). According to the displacement of the Litani river a Quaternary slip rate of ≈ 5 mm/yr has been inferred (Walley, 1988; Westaway, 2004).

Displaced landforms, such as faulted alluvial fans and wind gaps, illustrates that the Yammouneh fault has only experience a strike slip component in the late Quaternary (Gomez et al., 2006). According to Nemer and Meghraoui (2006), the Roum fault slips at a rate of 0.8 - 1.1 mm/yr based on the consistent offsets of small streams. Kinematic models using geodetic data provide us with present day slip rates. A recent plate model predicted a relative movement between the Arabia and Sinai plates to be 4.8 ± 0.4 mm/yr oriented N10W (Reilinger et al., 2006). This is to a certain extend consistent with the sum of the slip rates on the Yammouneh fault and the Serghaya/Rachaya fault suggested by Gomez et al., (2003). Geodetic slip rates were computed from a constellation of permanent and campaign GPS landmarks that have been measured continuously over a span of 4 years. The slip rates indicated 4-6 mm/yr, which is consistent with the 5.1 ± 1.3 mm/yr slip rate suggested by the geomorphologic approach.

Shortening rates:

  Compared to the strike-slip kinematics, the constraints on the shortening rate across the bend are still limited. Evidence of contraction is suggested by GPS data (Gomez et al. 2006) and coastal uplift generated by an offshore thrust belt (Morhange et al. 2006). According to Gomez et al. (2006), the LRB is currently active by a small component of horizontal shortening taking place between GPS landmarks located on opposite sides on the Yammouneh fault. The data processing suggested a 2 mm/yr component of shortening across the bend. This shortening rate is computed across the middle section of the Yammouneh fault along two different axes (Gomez et al. 2006). Folding and coastal uplift is also a manifestation of crustal shortening and thickening. In North Lebanon to the west of the Yammouneh fault along the Zagharta syncline, late Quaternary deposits

were found to be slightly back-tilted, signifying recent folding (Gomez et al. 2006). Notched shorelines in Northern Lebanon are higher than those along the Syrian Coast (Pirazolli et al., 1996). Uplifted notches are seen offshore of Tripoli indicating abrupt uplift of the Lebanese coast (Figure 1.3) (Nemer, 2005). According to Elias et al. (2007), a 100-150 km east dipping offshore thrust belt was discovered by sea beam bathymetry to the west of the LRB. Carbon (^{14}C) dates and precise biological sea level indicators revealed two significant abrupt regional crustal uplift episodes during the past 6000 years. The upper shoreline, with an uplift of 120-140 cm, is dated from 6000 to 3000 BC, while the lower shoreline, with an uplift of 80 ± 30 cm, is dated between the fifth and the sixth century (Morhange, 2006). Pirazzolli et al. (1996) suggested an uplift rate of 0.75-1 mm/yr inferred from notched shorelines.

Tectonic Rotations:

Tectonic settings within the LRB are believed to cause block rotations. In the case of the LRB, I'll be discussing the bookshelf rotation occurring on the western and the eastern side of the bend, localized rotation of local anticlines, and the regional rotation. To begin, paleomagnetic measurements conducted within the LRB yielded a counterclockwise (CCW) rigid block rotation of $61 ± 9.6^o$ (Ron, 1987). The sense of rotation is consistent with regional left-lateral shear and right lateral strike slip faults on secondary faults and block rotation (Figure 1.6 and 1.7). This style of deformation is believed to reflect a bookshelf rotation. Minor folds orientations are consistent with this bookshelf rotation. Fold hinge lines originally formed parallel to the orientation of the bend rotate with the bookshelf rotation. This is illustrated with the obliquely oriented Turbol anticline, which is supporting the previously discussed CCW rotation (Figure 1.8).

Moreover, according to Ron (1987 & 1990) a certain component of tectonic rotation exists on the flanks of Mount Hermon, which is also a CCW rotation. Paleomagnetic studies suggested rates of 69° ± 13° of CCW rotation (Ron 1987 and 1990) and a ~ 70° of CCW rotation (Gregor et al., 1974). This block rotation is caused by the fact that RcF and SF wrap around Mount Hermon and make it a rigid block (Gomez et al., 2003). The produced sense of rotation is consistent with what would be expected in a two sinistral fault system. Moreover, regional rotation has been reported in recently published studies. According to Reilinger et al., (2006), the Arabian plate is undergoing a CCW sense of rotation around a pivot point located in the Nile Delta. While according to other sources, the center of rotation has been gradually migrating from the mid-Mediterranean, to Crete island, and to its current location where it just lies off the Nile Delta (Eck and Hofstetter 1990).

Specific science questions include:

- Which of the main faults is/are locked and accumulating interseismic strain? How deeply locked are these faults?

- How do short term slip rates compare with late quaternary estimates?

- Is all slip from the southern DST section transferred to the Northern DST or partially dissipated elsewhere?

- Is shortening across the bend accommodated by the offshore thrust belt?

- Are present day rotations consistent with a typical restraining bend and the paleomagnetic rates?

- Is shortening across the bend accommodated by the offshore thrust belt?

- What is the hazard assessment and threat to mega-cities such as Beirut and Damascus with populations of ~ 1.5 and ~3.5 million respectively?
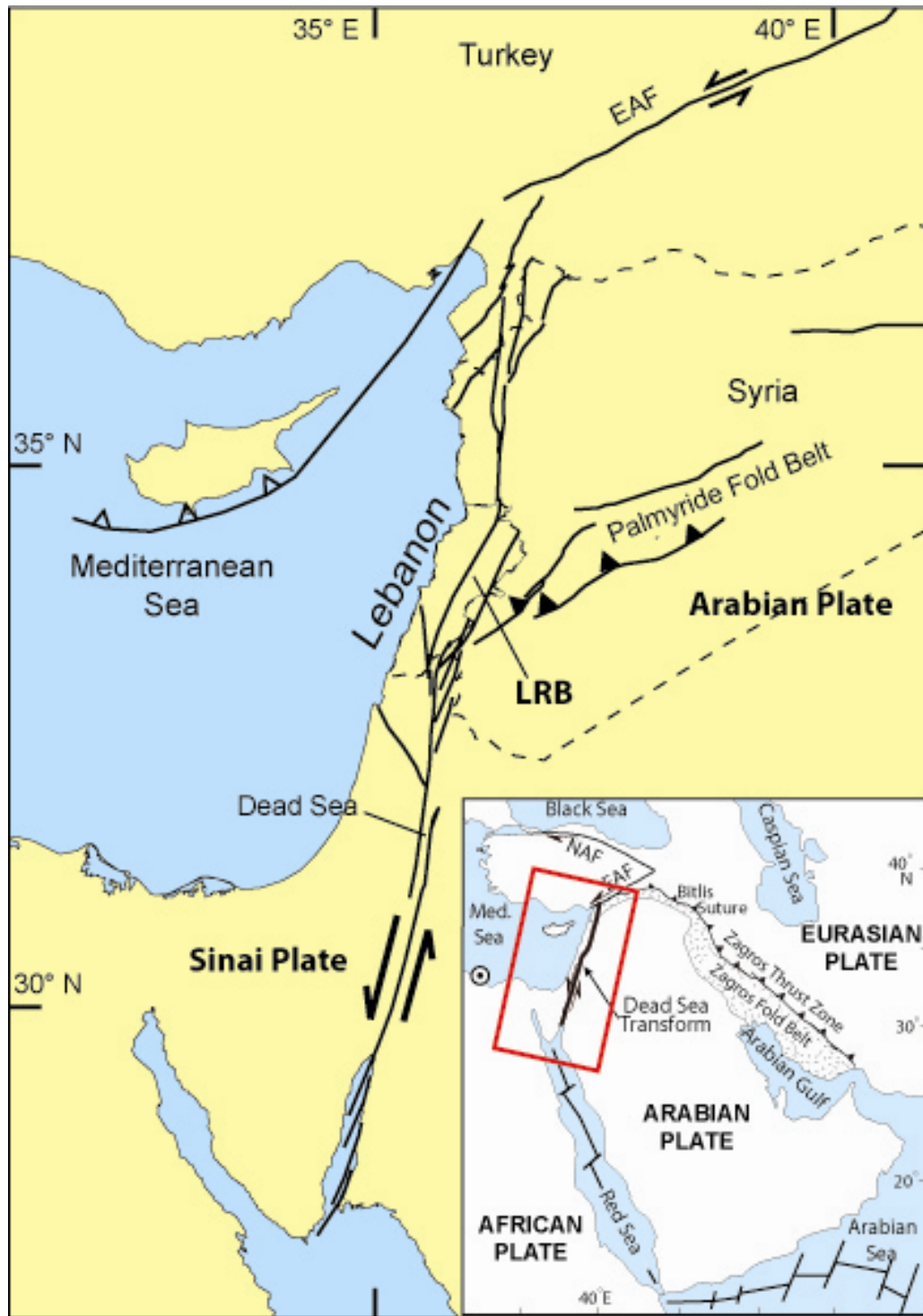
Figure 1.1: Regional tectonic map of the Dead Sea transform. Also shown is the sense of slip along the DST and LRB.
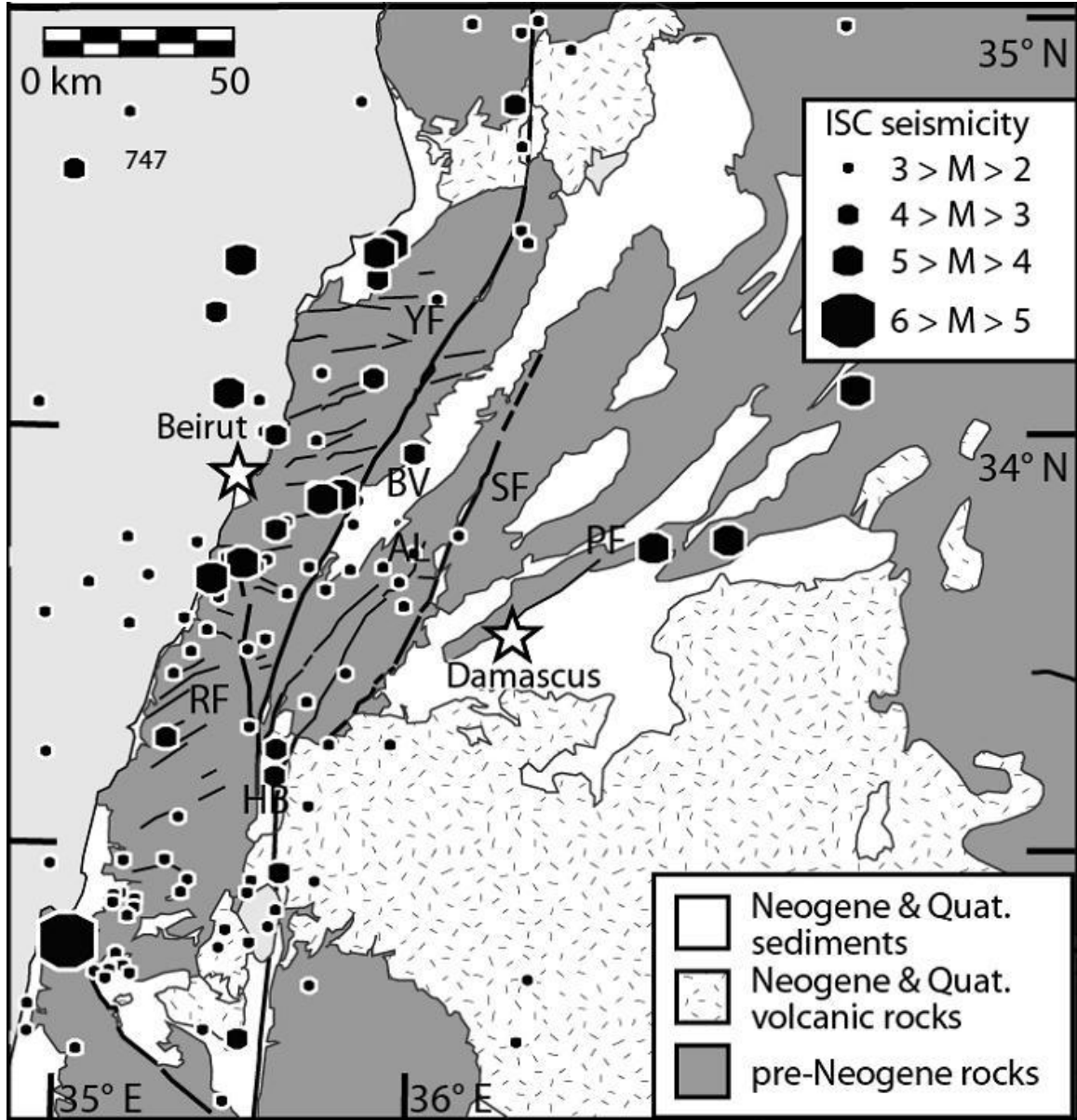
Figure 1.2: Instrumental seismicity from the Instrumental Seismological Center (1963-1997) representing events with 2 > M > 6.

Figure 1.3: Uplifted notches offshore of Tripoli (Courtesy of Tony Nemer)
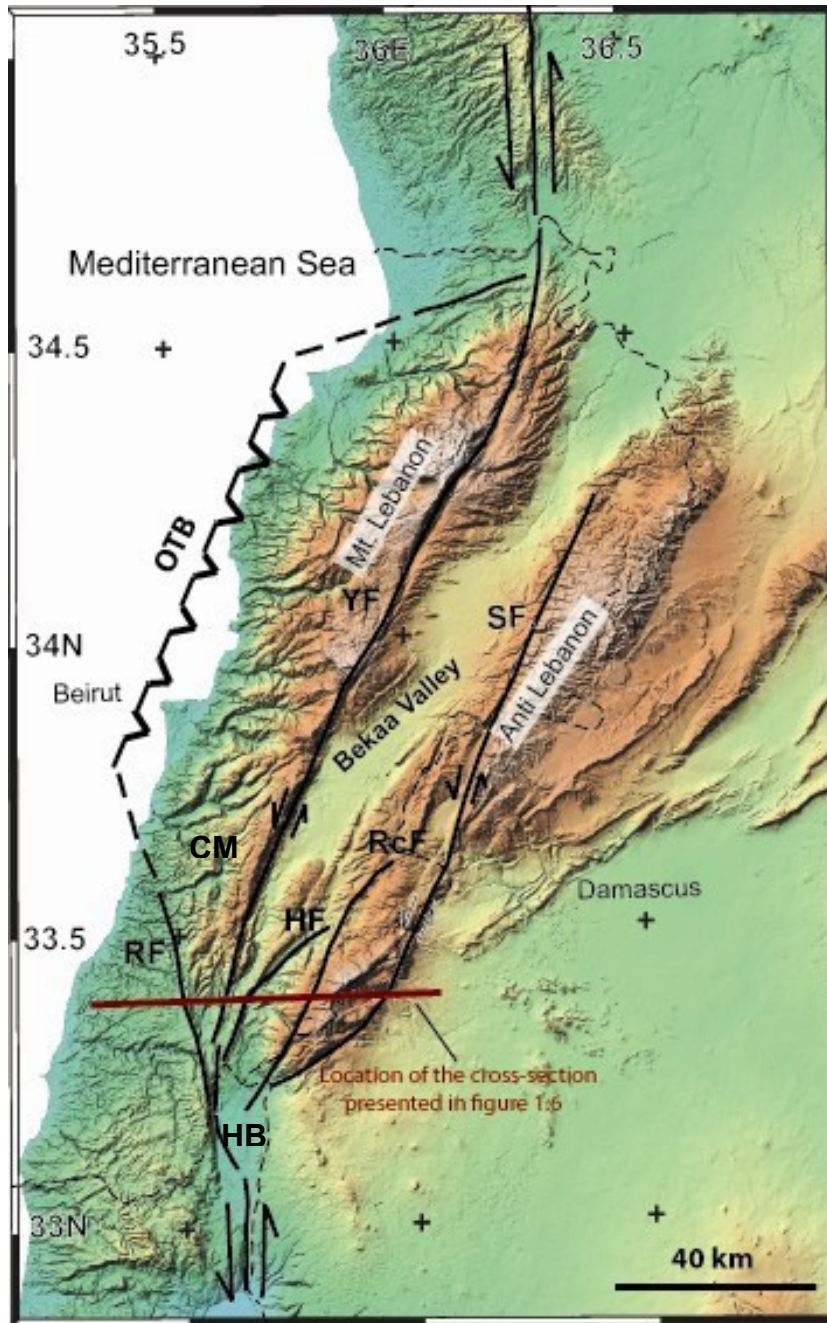
Figure 1.4. Major faults in Lebanon (CM= Chouf Monocline, HB= Hula basin, HF= Hasbaya fault, RcF = Rachaya fault, RF= Roum fault, SF= Serghaya fault, YF= Yammouneh fault, CF= Coastal Flexure, OTB= Offshore Thrust Belt, MF= Missyaf fault.
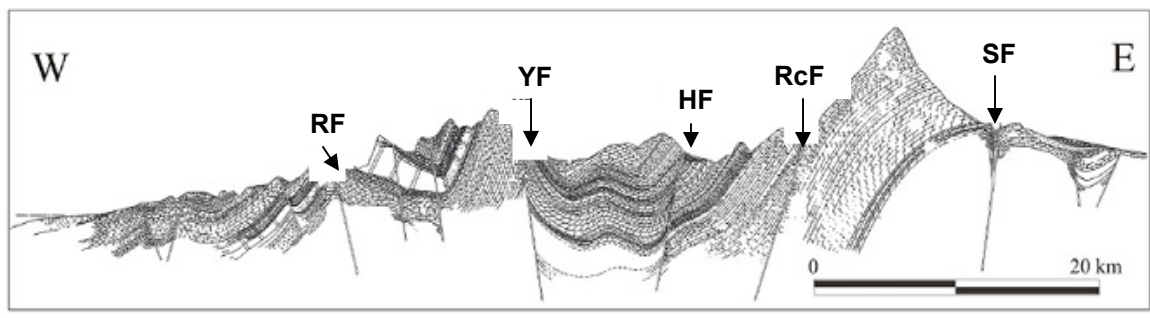
Figure 1.5: Cross section of the Southern part of the restraining bend. Location of the Transect is indicated on Figure 1.4 (Adapted from Sabbagh 1962).
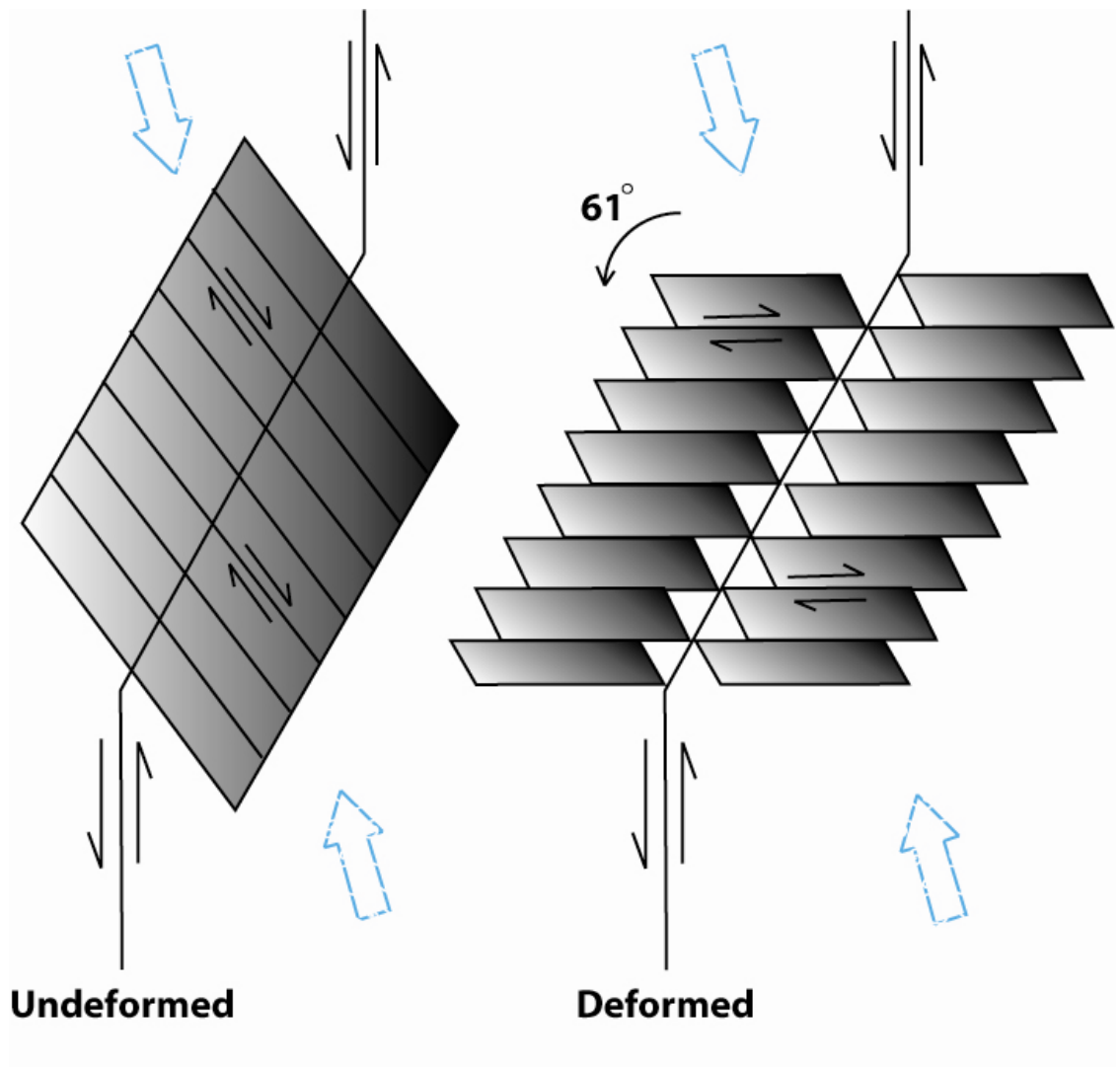
Figure 1.6: Conceptual geometric reconstruction of faulting and rotation within the LRB before (undeformed) and after (deformed) faulting using rotation rates suggested by Ron (1987).
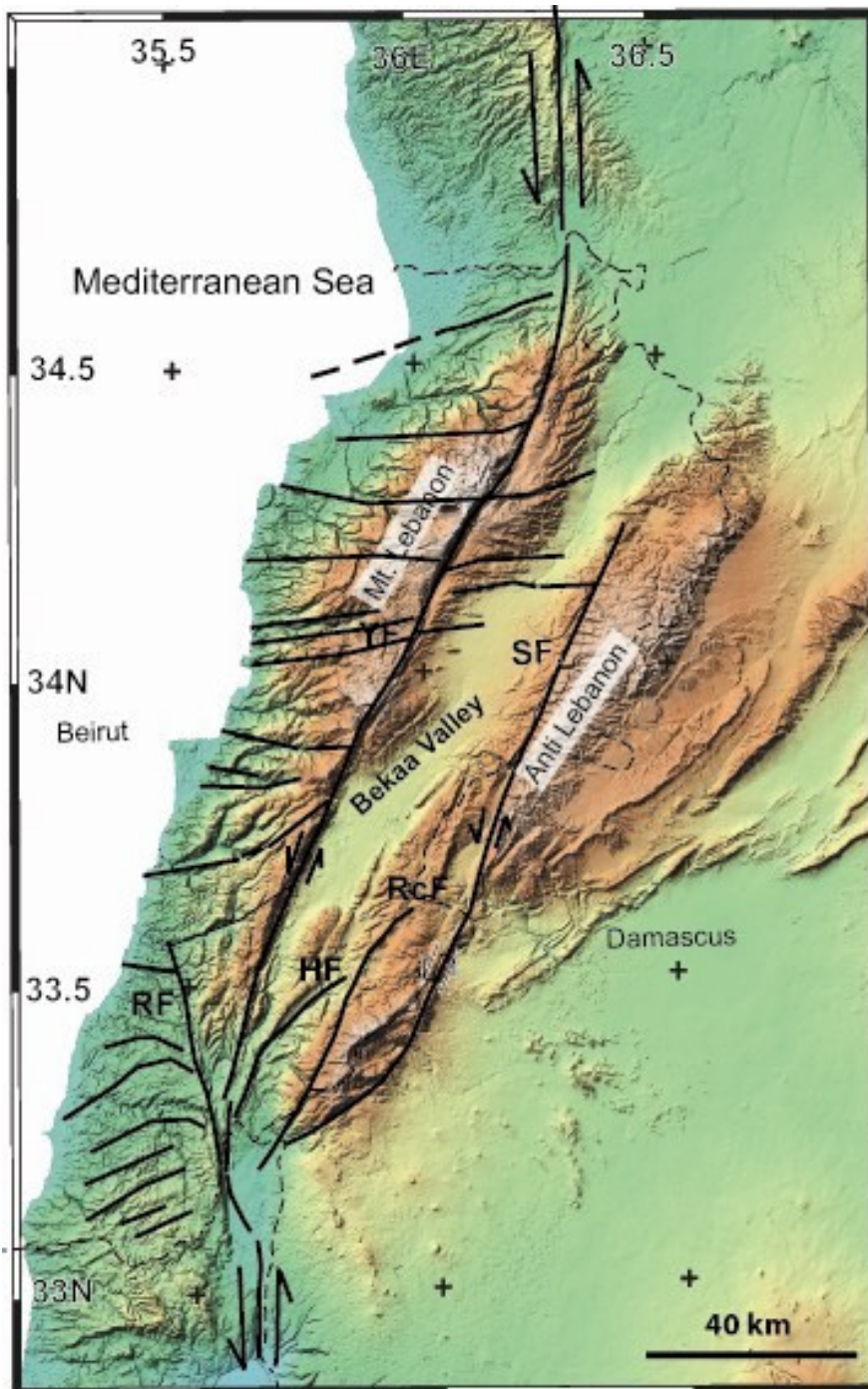
Figure 1.7: Showing the E-W striking faults within the LRB. Abbreviations: YF = Yammouneh fault, RF = Roum fault, HF = Hasbaya fault, and RCHF = Rachaya fault.
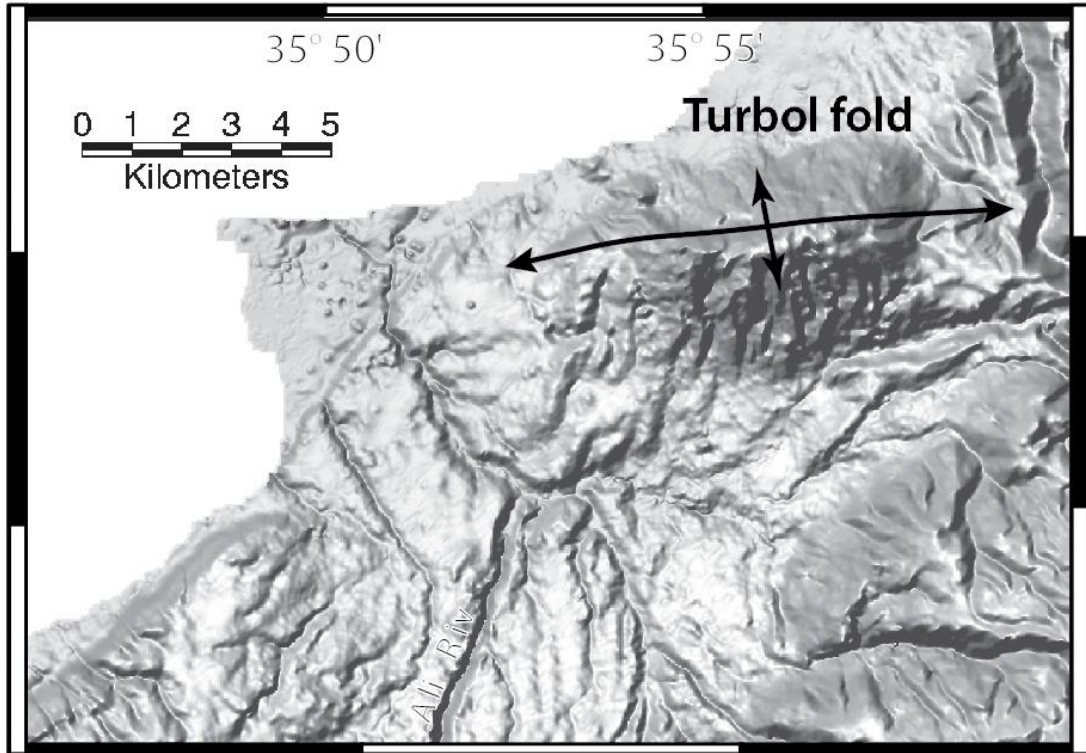
Figure 1.8: North of Lebanon region showing Turbol fold (Modified from Gomez et al. 2006).

Figure: 1.9: Jabal Terbol fold.   1.10: Vetical dipping layers.
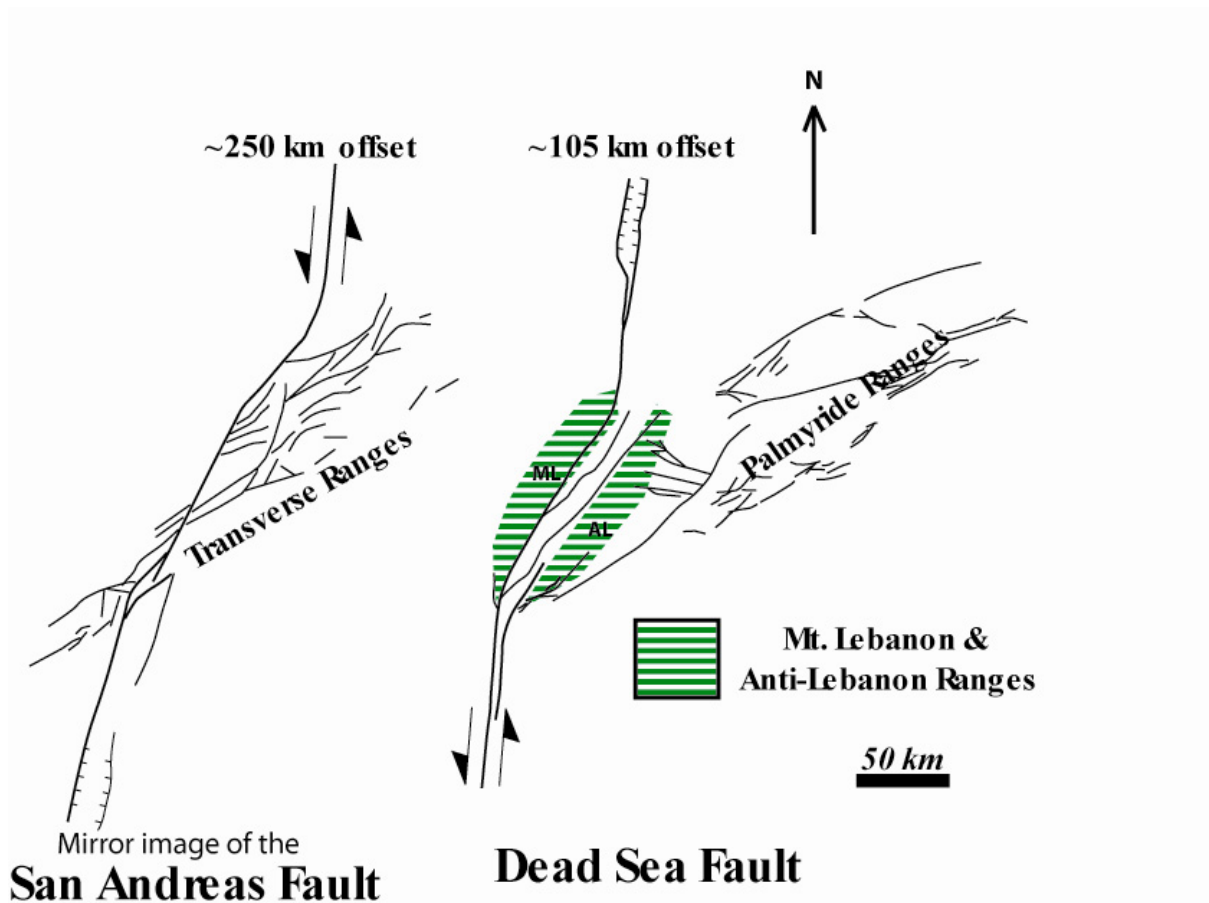
Figure 1.11: Comparative geometry between the LRB and the Big Bend of the San Andreas fault system in Southern California. The above presented San Andreas figure is a mirror image of the actual geometry for better comparison with the sinistral LRB. (Modified from Chaimov et al. 1992)

Chapter 2

The Global Positioning System (GPS)

What is the Global Positioning System?

The Global Positioning System (GPS) is designed by the US Department of Defense and is officially known as the Navigation Satellite Timing and Ranging (NAVSTAR). It has become a geodetic tool for studying a wide range of geophysical phenomena. GPS is used to determine the motion of earth's tectonic plates, study deformation around faults and volcanoes, measure the adjustment to earth's surface due to change in world's ice sheet, and contribute to atmospheric studies.

GPS provides three-dimensional relative positions with a precision of few millimeters. GPS provides a valuable tool in determining vertical as well as horizontal displacements. GPS measurements have accuracies of 2-5 mm in the horizontal direction and 6-15 mm in the vertical direction. It is relatively cheap when compared to other geodetic techniques such as: Very Long Baseline Interferometry (VLBI) and Satellite Laser Ranging (SLR).

The GPS system consists of four major components: the space constellation and broadcast signals, the control segment that is in charge of the system, the satellite signal properties, and the user segment including the different GPS receivers.

This chapter summarizes the main components of the GPS system and the basic aspects of GPS signal processing. For more detailed information, the reader is referred to Fadil, A. (2006), Herring et al. (2006), and Segall et al. (1997).

-Space Constellation:

The space constellation consists of 32 satellites placed in orbit at an elevation of 20200 km over earth's surface. These satellites are placed in 6 different circular orbit planes spaced about the equator at a 60 degree separation with an inclination of 55 degrees. The satellites have an orbital period of 12 hr. With such a constellation there would be at least

4 satellites visible above a 15 degrees cut-off angle at any given location on the earth's surface at any given time. Also, the satellites in orbit consist of three different generations: Block I, Block II/IIa, and Block IIR that can measure distances between satellites and compute ephemeris on board. Signals are sent from the satellites in orbit to the users at two different frequencies of L1 = 1575.42 MHz and L2 = 1227.60 MHz, while the ones sent to the control segment are received at a frequency of 1783.74 MHz.

-GPS control segment:

The control segment currently consists of one master control station (MCS), five monitoring stations, and four ground antennas distributed within the vicinity of the equator at four various localities. The MCS receives signals from satellites and monitoring stations, pre-computes satellites ephemerides, control the behavior of satellite clocks and formulates the navigation data. Once the previous steps are accomplished, the data is broadcasted back to the satellites in view via the ground antennas. The Master Control Station is situated in Falcon Air Force Base in Colorado Springs, Colorado.

-Satellite signal properties:

The NAVSTAR GPS is a one way ranging system where signals are only being transmitted from the satellite. This means that a clock reading at the transmitter antenna (satellite) is compared with a clock reading at the receiver antenna. Each satellite transmits data on two different frequencies, L1 and L2 (Wavelength: L1 ≈ 19.0 cm and L2 ≈ 24.4 cm). The reason for the second signal L2 is for self calibration of the delay in the earth's ionosphere. The coarse acquisition code (C/A) can be found on L1 and contains the time according to the satellite clock when the signal was transmitted. For recognition purposes, each one of the satellites has a different C/A code. The P-code is identical on both bands (L1 & L2) and is more for precise positioning. The P code carries

identical information as the C/A code, but has ten times the resolution of the C/A code

(1.023 MHz vs. 10.23 MHz). Moreover, the L1 band carries the Navigation message.

This message consists of the ephemeris information, predicted GPS satellite orbits &

clock corrections, ionospheric model, satellite health status, and flags on each satellite

indicating whether the anti-spoofing (A/S) is on. The A/S is an encryption of the P-code.

Furthermore, the A/S does not cause a problem to the precise user, since precise GPS

procedures rely on measuring the phase of the carrier signal itself rather that

pseudorange. Pseudorange is the measurement of the distance between a satellite and a

navigation satellite receiver.

Pseudoranges are very useful in the rapid position fixes required by moving vehicles

and kinematic surveying. The pseudorange measures the distance between the satellite

and the antenna by computing the time it takes the signal to propagate from the satellite

to the receiver. In other words, the pseudorange is the time offset that is necessary to

correlate the incoming code sequence with a code sequence generated in the GPS

receiver, multiplied by the speed of light and that would result in an error value up to $\pm$ 3-

6 m:

$$p = \rho + c * (dt - dT) + d_{ion} + d_{trop} + \varepsilon_p \qquad (2.1)$$

Where p is the pseudorange, ρ is the geometric range to the satellite where the receiver

coordinates are hidden, c is the speed of light, $dt - dT$ is the offset between the satellite

and the receiver clocks, d_{ion} and d_{trop} are the ionosphere and troposphere delays, and ε_p

represents the effect of multipath and receiver noise.

The carrier phase is more accurate than the pseudorange. It is the phase of the received

carrier with respect to the phase generated by an oscillator in the GPS receiver. This

phase difference is called the carrier beat phase which is translated to a number of fractional phase, since the carrier has a frequency with a cycle rate about 1000 times faster than the receiver. Once done, this carrier beat phase is converted into a distance (number of fractional phase multiplied by carrier wavelength) and is added to the to the pseudorange value to give us the carrier phase (Herring et al., 2006):

$$\Phi = \rho + c * (dt - dT) + \lambda * N + d_{ion} + d_{trop} + \varepsilon_p \qquad (2.2)$$

Where Φ is the carrier phase, N is the number of fractional phase, and λ is the carrier wavelength.

GPS receiver:

The primary components of a standard GPS receiver are: antenna, radio frequency section, microprocessor, control and storage device, and power supply.

GPS coordinate system:

There exist two types of coordinate systems: The Celestial and the terrestrial systems. To begin, the Celestial is needed to describe the satellite motion in space. It uses the quasars for reference and it is more known as the International Celestial References Frame Observations. Then, the terrestrial system is used to obtain the coordinates of positions on the ground. Terrestrial coordinate systems like the International Terrestrial Reference Frame (ITRF) and the World Geodetic System (WGS 84). The WGS 84 is the most widely used global reference system because it is the system in which the GPS satellite coordinates are expressed in the navigation message.

GPS errors:

There exist a variety of sources affecting the error level with the GPS readings. First, the receiver and satellite clock bias produces an error component. The satellite clock bias

is a systematic error, while the receiver clock bias is the difference between the GPS time and the receiver clock time. Then, we have errors generated from satellites orbital errors. Also known as an imperfect broadcast orbital parameters. This would result in an incorrect satellite location and eventually in inaccurate GPS readings. This error is caused by gravity, radiation pressure, atmosphere effects, geoid modeling, solid earth, and ocean tides. Also, an error results when the center of the antenna and the electrical center of the antenna do not coincide, and when the phase centers for L1 and L2 do not overlap. Furthermore, the multipath is an important source of error and a serious concern for GPS users. This phenomena is when a GPS signal bounces off a reflective surface prior to reaching the GPS receiver antenna. The multipath can cause errors up to 15 cm for carrier phases and 15-20 m for pseudoranges. In addition, the ionized gases in the ionosphere result in changing the signal propagation speed as compared to that of free space. This results in a delay in the GPS code pseudorange and an advance in the carrier phase. The error in this case increases at low angles of propagation and during afternoon time. Further, the troposphere extends 50 km above the surface of the earth and this lower part of the atmosphere results in lengthening the propagation path due to refraction and thus resulting in an error component. The error value normally varies between 2.5 m at a 90° satellite elevation angle and 10-15 m at low satellite elevation angles. The ionospheric propagation error is the same for pseudorange and the carrier phase components. Next, electronic noise on the signal and within the receiver components can add additional error to the calculated position. This noise varies with the quality and design of the receiver, interference from other radio signal sources, temperatures and other variables. The error resulting from electronic noise could be as high as about 2 meters.

Methods to help reduce error values and error components include:

   Linear combinations are one approach to obtain GPS coordinates with significantly reduced errors. To begin, two different receivers tracking the same satellite would eliminate the satellite clock error. Also, one receiver tracking two satellites results in removing the error generated by the receiver clock. Then, when two receivers track two satellites, this eliminates both the receiver and satellite clock offset.

   The linear combination of the L1 and L2 phase measurements, which is known as the LC (ionosphere free) combination, reduces the effect of the ionosphere, but may amplify other sources of error (Herring et al., 2006). For short baselines (<10 km) LC can be treated as zero.

$$_{lc} = [(f^2_{L1}) / (f^2_{L1} - f^2_{L2})] * \Phi_{L1} - [(f^2_{L2}) / (f^2_{L1} - f^2_{L2})] *)] * \Phi_{L2} \qquad (2.3)$$

 The wide-lane and narrow-lane combinations are applied for ambiguity resolution.

$$_{wl} = (\Phi_{L1} / \lambda_{L1}) - (\Phi_{L1} / \lambda_{L1}) \qquad (2.4)$$

$$_{NL} = (\Phi_{L1} / \lambda_{L1}) + (\Phi_{L1} / \lambda_{L1}) \, m \qquad (2.5)$$

$$_{WL} = c / (f_{L1} - f_{L2}) \approx 0.86 \text{ m} \quad \& \quad _{NL} = c / (f_{L1} + f_{L2}) \approx 0.11 \text{ m} \qquad (2.6)$$

   Differential correction techniques are used to enhance the quality of location data gathered using global positioning system (GPS) receivers. This technique could be applied in real-time directly in the field or when processing the data at a later stage.

  Ultra high precision GPS are another way to achieve accurate obtained GPS coordinates. There exists three software capable of achieving that: Bernese, Gamit/Globk, and Gipsy.

GAMIT/GLOBK

GAMIT/GLOBK (Herring et al., 2006) is a comprehensive GPS analysis package developed for estimating station coordinates and velocities, functional representations of post-seismic deformation, atmospheric delays, and satellite orbits (Herring et al. 2006). GAMIT estimates station coordinates for each day in a loosely constrained solution. This means that the coordinates of the tracking sites and the GPS satellite orbits are not firmly constrained (final precise orbits have been used in the processing). In other words, the orbits of GPS satellites and station coordinates are not in a well determined reference frame. The baseline length is determined very precisely and the GPS network and constellation can be rotated and translated as a rigid body. A number of input files are needed in order to reach the desired accurate output, and these files are as follows:

- sestbl. and sistbl. (The session control tale that contains the GAMIT analysis command).

- process.defaults (specifies the computation environment, sources for internal and external data and orbit files, start time and sampling interval, and instruction for archiving the results)

- sites.defaults (lists the permanent and continuous GPS stations to be used and how station log data are to be handled)

- station.info (includes receiver, antenna type, and height of instrument for all stations in use)

- itrf00.apr (contains the cartesian coordinates of stations we wish to have unchanged throughout the processing)

- lfile. (encloses the cartesian coordinates of stations we wish to have updates after every day of processing)

- autcln.cmd (identifies and flags possible jumps in phase data)

- Rinex files (contains the GPS readings)

- Orbit files

- Navigation files

GLOBK is a Kalman filter whose primary basis is to combine solutions from the processing of geodetic data. It is an efficient recursive filter that estimates the state of a dynamic system from a series of incomplete and noisy measurements. This means that only the estimated state from the previous time step and the current measurement are needed to compute the estimate for the current state.

The primary input to GLOBK is the loosely constrained solutions from GAMIT processing. The three main features in GLOBK package are:

- glred (generates a time series of station coordinates in order to indentify and remove any survey days or stations which are outliers)

- globk (estimates the station coordinates averaged over a multi-day experiment by combination of individual sessions of observations, and at a later stage the station velocities from combination of averaged station coordinates obtained from several years of observations)

- glorg (stabilizes to best align estimated station coordinates and velocities with prior values for a selected set of stabilization stations)

Chapter 3

Results and Implications

Although neotectonic studies at specific locations have confirmed the activity of faults within the LRB, the present-day kinematics and strain transfer through the LRB is poorly constrained. To address this gap in our knowledge, this study presents near-field GPS velocity estimates for the LRB, new kinematic models that quantify the accumulation of interseismic strain and velocity gradients along the restraining bend, and discusses tectonic and earthquake implications.

GPS Measurements and data processing:

This study used GPS observations from survey-mode GPS sites, as well as continuous GPS stations in the region. Survey mode GPS campaigns spanned more than 5 years (April of 2002 until August of 2007) for the first generation Lebanese sites, ~ 2 years (December of 2005 until August of 2007) for the second generation Lebanese sites, and 7 years (2000 until 2007) for the Syrian sites. The Lebanese sites have been surveyed on a yearly basis compared to the Syrian sites that were just surveyed on two occasions in 2000 and 2007. In total, the GPS network of campaign sites is composed of 27 sites installed in bedrock, with 22 located within Lebanon (14 first generation & 8 second generation sites) and 5 located east of the LRB in SW Syria. In addition, two continuous GPS stations are located in Jbeil Lebanon (LAUG) and Damascus Syria (UDMC). During each campaign, sites were at least observed for 24 hours using Trimble 5700 GPS receivers with Zephyr Geodetic Antennae and fixed antenna masts for the Lebanese sites and tripods for the Syrian sites.

Raw GPS campaign data were processed along with other continuous stations in a two-step procedure (explained in Chapter 2) using the GAMIT/GLOBK software (Herring et al. 1997). Velocities were stabilized using the global ITRF2000 reference frame core sites

Figure 3.1: Fixed height mast with Zephyr antennae installed at HZRT.

and a "random walk" error of 1 mm/sqrt[yr] is assumed in the final velocity estimation. The "random walk" process noise value is assigned to stations in order to account for correlated errors in the time series (Reilinger et al., 2006). After stabilizing the reference frame, the station velocities are transformed to an Arabian-fixed reference frame, which allows better local tectonic interpretation of the bend.

Results and modeling:

GPS velocity map:

The resulting GPS velocities have 1-sigma uncertainties for the survey-mode sites as follows: less than 0.75 mm/yr for most of the primary Lebanese survey sites, less than 2.0 mm for the secondary Lebanese survey sites, and less than 0.5 mm for the Syrian survey sites and continuous stations (Table 3.1).

As shown in figure 3.2, sites located west of the LRB, along the Lebanese coast, are generally moving SSW with respect to the Arabian plate, and the velocities generally decrease toward the Arabian plate, which suggest locked faults accumulating strain. Velocity vectors parallel the bends orientation within the vicinity of the LRB. Particularly noteworthy, velocities tend to decrease in the northern part of the bend and appear to be in agreement with the lower velocities observed in the Syrian stations north of the bend. Figure 3.3 (a & b) graphically represents the displacements of the GPS stations taken place along the strike of the bend (NNE-SSW) and the displacement across the strike of the bend (WEW-ESE). The profile across the strike of the bend displaces a sinistral sense of slip with a non-creeping locked fault.

GPS_site	Long. (deg)	Lat. (deg)	ITRF 2000		ARABIA-fixed		1-σ E	1-σ N	Correlation
			Vel E (mm/yr)	Vel N (mm/yr)	Vel E (mm/yr)	Vel N (mm/yr)			
Primary Lebanese survey sites									
ARSL	36.467	34.174	-1.19	-0.04	-1.18	-0.04	0.68	0.68	-0.011
HRML	36.369	34.412	-0.45	0.05	-0.45	0.06	0.76	0.71	0.028
TFEL	36.235	33.860	-1.60	0.86	-1.61	0.86	1.15	1.15	-0.004
BRKA	36.143	34.194	-1.39	-0.48	-1.38	-0.48	0.60	0.62	-0.008
HABT	36.084	34.461	-0.77	-0.99	-0.77	-0.99	0.53	0.53	-0.007
ANJR	35.922	33.740	-0.69	-1.19	-0.69	-1.19	0.60	0.61	0.000
ADAS	35.899	34.466	-0.96	-1.06	-0.96	-1.06	0.54	0.54	-0.004
HZRT	35.880	33.859	-2.18	-0.28	-2.19	-0.28	0.64	0.63	-0.007
FRYA	35.829	34.015	-1.02	-1.44	-1.02	-1.44	0.62	0.62	0.020
HAYT	35.762	34.089	-2.40	-2.19	-2.40	-2.19	0.59	0.59	-0.002
MCHK	35.761	33.516	-1.79	-0.97	-1.79	-0.97	0.56	0.56	-0.004
JZIN	35.579	33.545	-1.16	-1.93	-1.16	-1.94	0.58	0.59	-0.001
JIYE	35.401	33.641	-1.80	-2.53	-1.80	-2.52	0.66	0.65	-0.020
RBDA	35.162	33.149	-0.51	-3.21	-0.51	-3.21	0.69	0.70	-0.005
Secondary Lebanese survey sites									
TANR	35.910	34.183	-1.53	1.57	0.17	0.09	1.86	1.87	-0.020
KOUK	35.902	33.531	-1.87	0.09	0.16	0.09	1.61	1.65	-0.018
ARNA	35.532	33.323	-0.93	-2.26	0.16	0.10	1.55	1.56	-0.003
ENFE	35.748	34.352	-2.65	-0.19	0.14	0.08	1.40	1.47	-0.033
ZARA	35.302	33.365	-0.56	-0.45	0.16	0.09	1.57	1.61	-0.034
CHAR	35.588	33.742	-4.07	-1.85	0.14	0.08	1.33	1.35	-0.032
Syrian survey sites									
MSHR	36.550	34.059	1.42	0.63	0.12	0.07	0.57	0.54	-0.013
ASAL	36.400	33.879	1.27	0.81	0.13	0.07	0.59	0.56	-0.026
HOOR	36.111	33.781	0.56	1.00	0.13	0.07	0.60	0.59	0.024
SOBA	36.051	33.613	0.55	0.85	0.13	0.07	0.50	0.49	-0.011
ROZA	36.010	33.625	-0.72	0.24	0.13	0.07	0.59	0.59	-0.031
Continuous stations									
ELRO	35.771	33.182	-0.34	-0.80	-0.34	-0.80	0.41	0.40	0.002
UDMC	36.285	33.510	-0.92	0.52	-0.93	0.52	0.47	0.46	0.002
LAUG	35.674	34.115	-1.47	-2.08	-1.47	-2.08	0.51	0.51	0.004
KABR	35.145	33.023	-1.44	-2.60	0.25	0.05	0.41	0.40	0.002
BSHM	35.023	32.779	-0.98	-3.23	-1.56	3.25	0.40	0.40	0.002

Table 3.1: Velocities of GPS sites shown in figure 3.2.
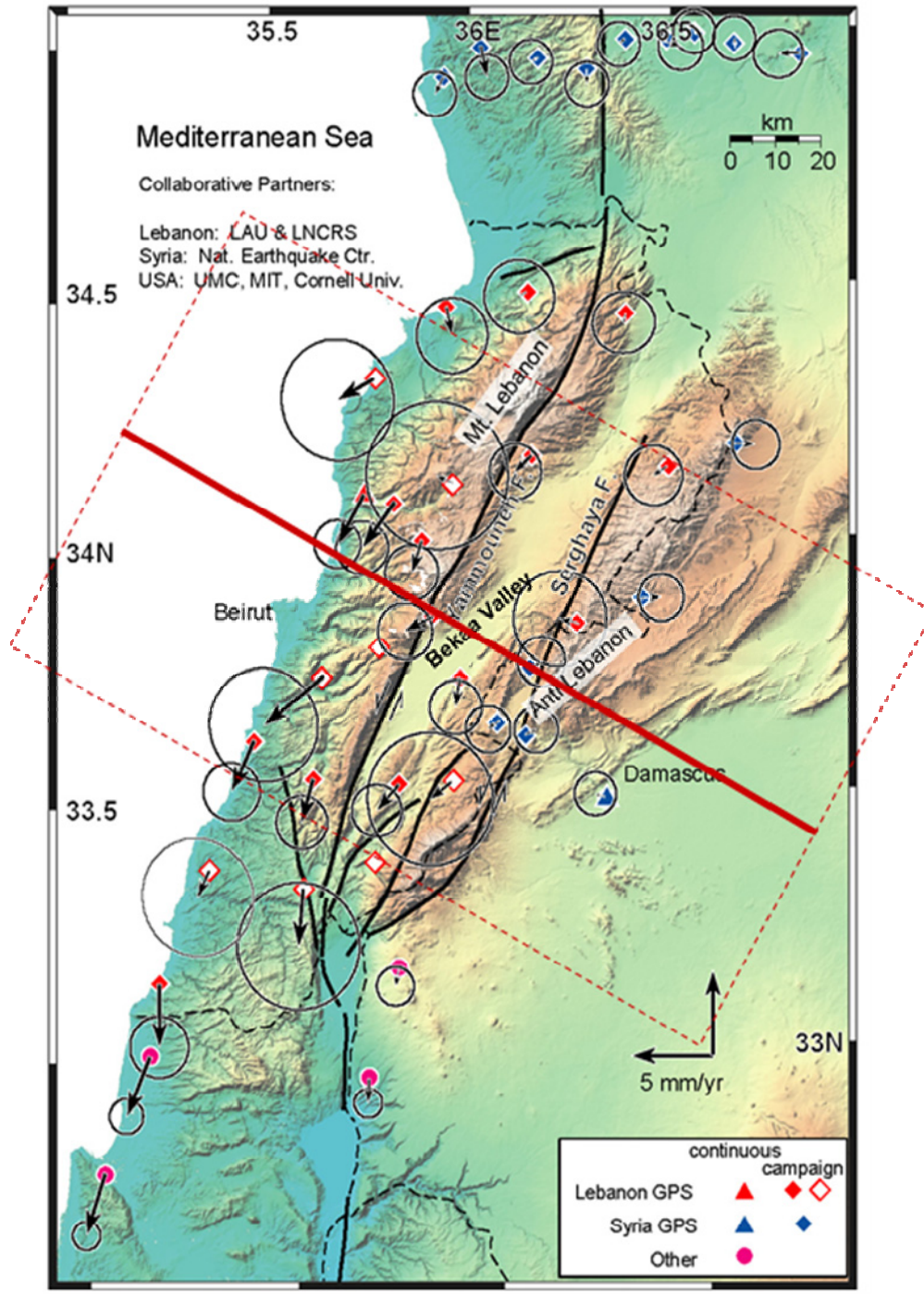
Figure 3.2: Map showing general structure of the LRB. GPS velocities for the network used in this study are also shown in an Arabian-fixed reference frame (1 sigma uncertainties). The red box indicates the stations plotted in the profiles of figure 3.3, 3.4, and 3.5.

A **Displacement parallel to the fault**

B **Displacement normal to the fault**
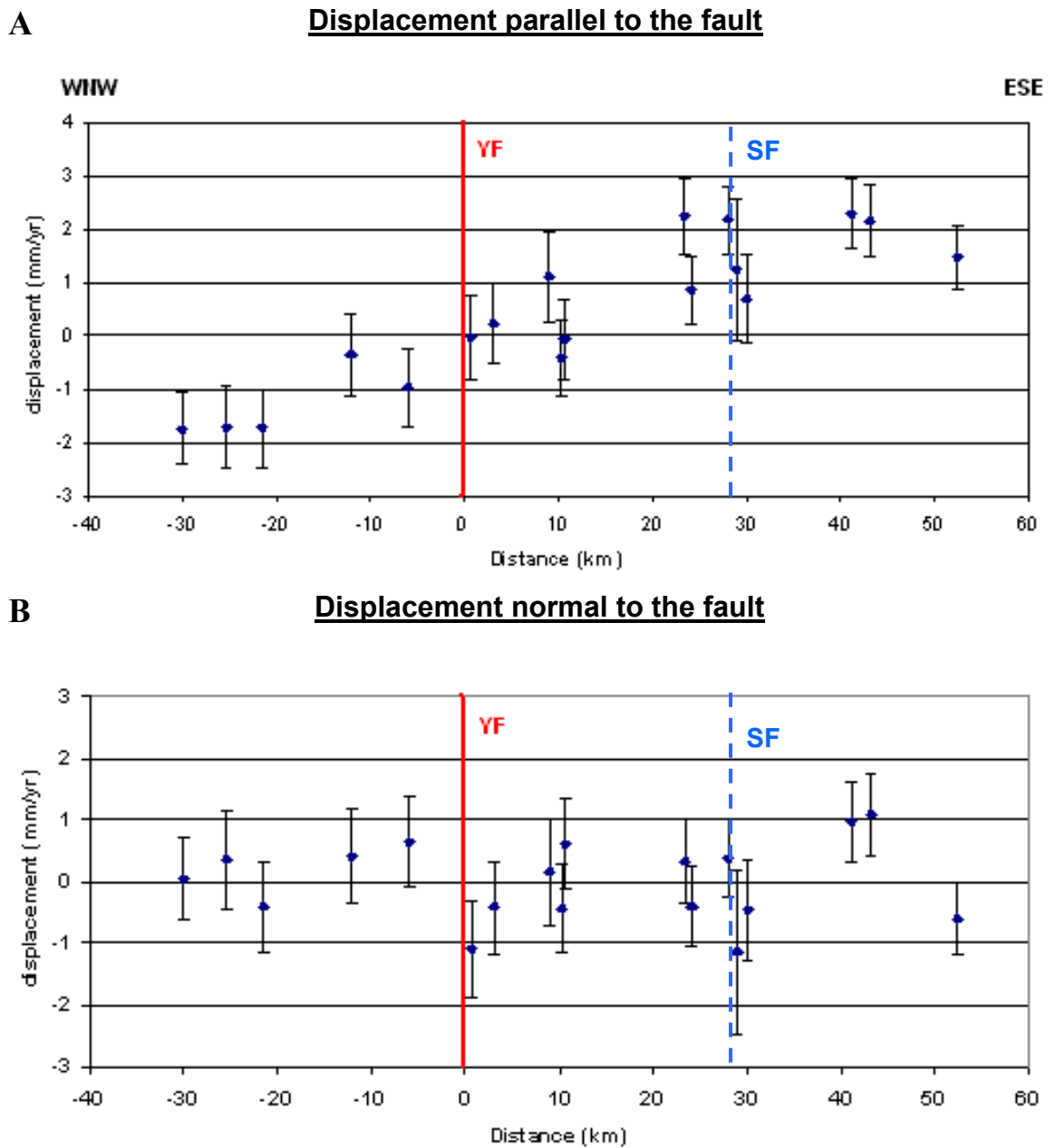
Figure 3.3: Plot showing GPS velocities (A) parallel and (B) perpendicular to the Yammouneh fault across the central part of the LRB. Positions are plotted relative to the Yammouneh fault (YF).

Velocities perpendicular to the restraining bend demonstrate no statistically significant shortening across the bend. This contrasts with 3.1 ± 0.4 mm/yr of convergence across the LRB that is suggested by regional plate tectonic models (e.g; Reilinger et al. 2006).

One possibility is that shortening is accommodated outside the aperture of the GPS network, specifically offshore Lebanon. This is similar to the observation and conclusion of Lisowski et al. (1991) for the big bend of the San Andreas fault. They suggested that convergence is not concentrated at the bend but is instead accommodated elastically over a broad zone and apparently released by faulting in that same zone. Offshore Lebanon, a recent Marine survey has identified recent folding (Elias et al. 2007).

The resulting GPS velocity field provides a basis for kinematic analyses of the DST within the Lebanese restraining bend. The modeling strategy is as follows:

(1) 1-D elastic dislocation model: This provides an initial constraint on the slip rate and locking depth. Although a 2-D elastic dislocation model is more appropriate and realistic for the LRB, 2-D models cannot easily constrain both the slip rate and the fault locking depth.

(2) 2-D elastic dislocation model: Using the best estimate of locking depths, refine the slip rate allowing for strain partitioning, variable fault geometry, and modeling strike slip faults in addition to thrust faults.

(3) Velocity-gradient analysis: A means of assessing infinitesimal deformation, such as dilatations, rotations, and strains.

1-D elastic dislocation model:

The displacements exhibited by the profile striking WNW-ESE (Figure 3.3.A) compare well with the general pattern predicted by elastic dislocation models for a locked strike-slip fault (e.g; Savage and Burford 1973). An initial model involves a 1-D (profile) model that assumes an infinitely long strike slip fault. This 1-D model is useful as a start because it has a simple analytic relationship that relates the velocity of a point (v) to distance normal to the fault (x) as:

$$v = (b/\pi) \ arctan \ (x/D) \qquad\qquad (3.1)$$

where b is the long-term slip rate and D is the locking depth (Savage & Burford 1973).

For this 1-D model, the inverse model finds the best b and D (slip rate and locking depth) for a set of observed velocities (v & x).

Single fault model:

Considering the uncertainties in GPS velocities, a 1-D dislocation model was initially applied allowing for only a single fault system, the Yammouneh fault (YF). The inverse model was implemented by adopting a grid search to obtain the slip rate and locking depth with the lowest WRMS (weighted root mean square). The grid search weights each of the sites inversely proportional to the square of its uncertainty (Gomez et al., 2007). The 1-sigma ellipse shown in figure 3.5 is based on a Monte Carlo analysis, which is a computational algorithm that allows the noise of the data to be considered (e.g. Sandvol and Hearn 1994) and was obtained after performing 1000 iterations.

The plot shown in figure 3.4 corresponds to the 5.6 mm/yr slip rate and 28 km locking depth with the lowest WRMS.
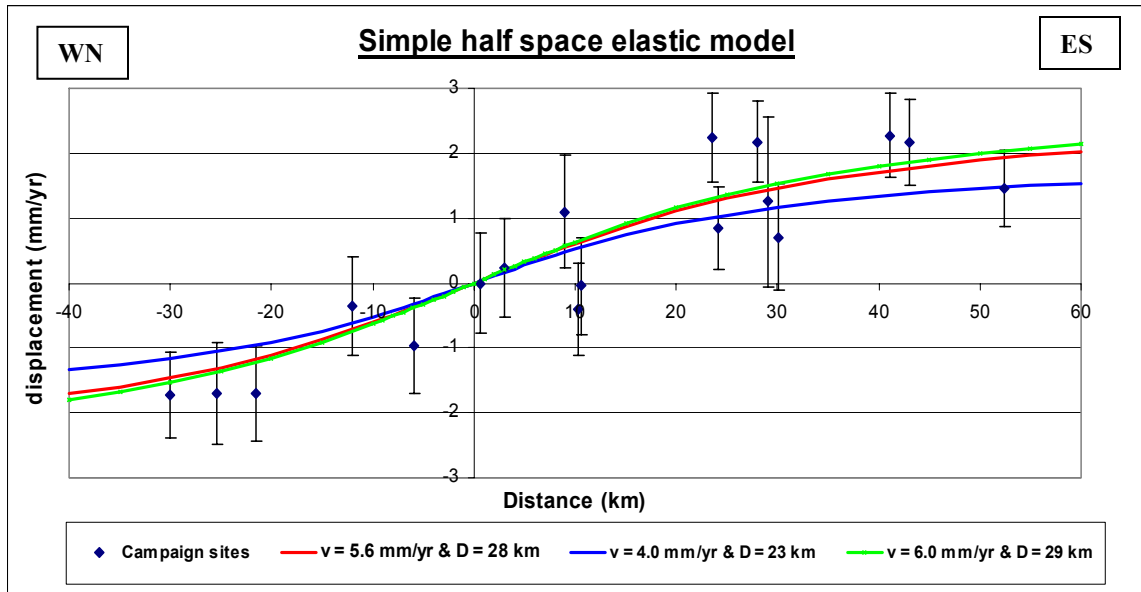
Figure 3.4: Simple half space elastic dislocation model considering a single fault system (YF). The red profile corresponds to the best fit slip rate and locking depth obtained from the grid search (lowest WRMS). The blue and green profiles correspond to the upper and lower limit of slip rates along the YF (~ 4 mm/yr & 6 mm/yr). The locking depth values indicated for the blue and green profiles were obtained from a linearized least-square regression.
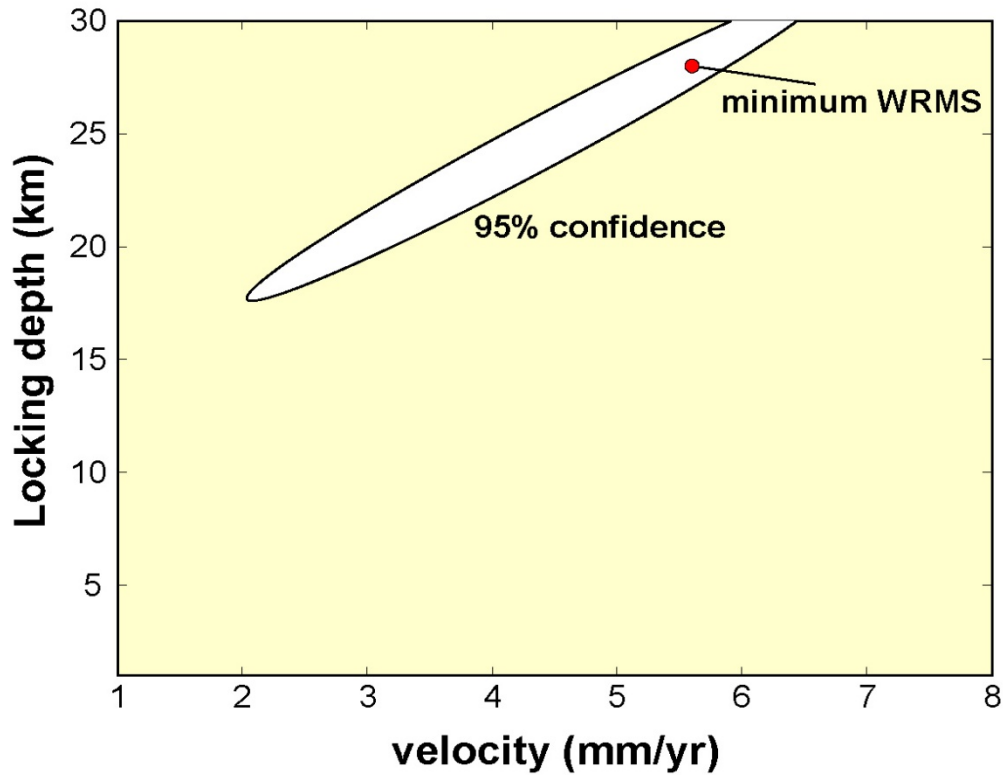
Figure 3.5: Plot showing the 1-sigma confidence limits on slip rate and locking depth in a single fault system (YF). Confidence limits are based on a grid search approach and a Monte Carlo analysis to evaluate the noise level in the data.

The 5.6 mm/yr slip rate corresponds to the upper range of the 5.1 ± 1.3 mm/yr rate provided by Daeron et al. (2004) and the 5.0 ± 1.1 mm/yr rate provided by Gomez et al. (2007). Although locking depth does not necessarily correspond to a real layer in the crust (e.g. brittle-ductile transition), 28 km is generally a large value considering that the crust thickness in Damascus is 35 km (E. Sandvol, personal communication). Also, a Moho depth of 30 to 31 km in the Bekaa was suggested by Tiberghien (1974) from gravity data. Not surprisingly in the 1-sigma confidence limit, a high covariance exists between locking depth and velocity values. The slip rates ranged from 2 to 7 mm/yr, whereas locking depth values ranged from 17 to over 30 km (figure 3.5). The slip rates of 2-2.5 mm/yr are slower than actual geological slip rates, but correspond to more acceptable and realistic locking depth values (17-18 km).

<u>Double fault model:</u>

The 28 km locking depth obtained in single fault model is an indication of broadly distributed strain away from the fault (i.e.: locking depth should not be taken as a literal depth). Introducing multi-dislocations can broaden the strain distribution and produce shallower and more acceptable locking depths. Since the SF is known to be active, a two-fault model (YF and SF) may be justified. For this approach, a linearized least-square regression was adopted to find slip rates on two faults spaced by 28 km (YF and SF) by trying different locking depth values. Assigning D values to best match the 1.4 ± 0.2 mm/yr along the SF and 4.1 mm/yr along the YF suggested by Gomez et al., (2003) resulted in a D = 15 km and slip rates of 3.8 mm/yr and 1.1 mm/yr. This 15 km is a reasonable D values with a 30^+ km crust (figure 3.6), and is consistent with the 15 km locking depth value adopted in previous dislocation models (Reilinger et al 2006). This two fault model is poorly constrained because of much variability among the strike slip
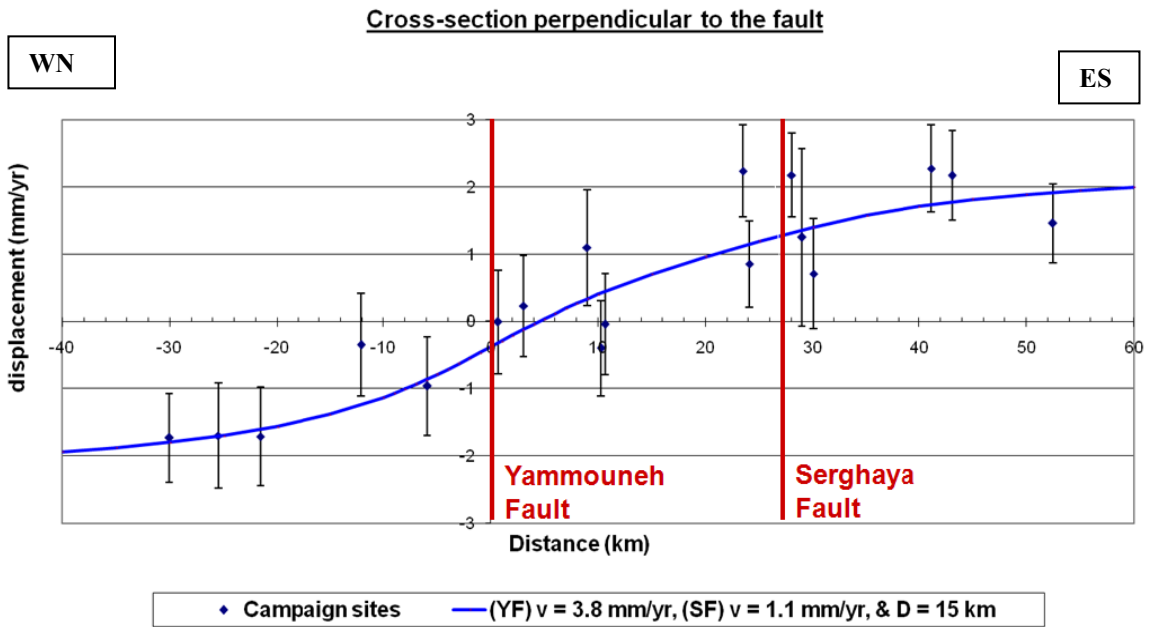
Figure 3.6: Simple half space model considering a double fault system (YF and SF). The profile indicates the predicted slip rates with the lowest WRMS for the YF and SF that best match the geological rates of the YF and SF. Slip rates were achieved by a linearized least-square regression where a range of locking depths was considered.

distribution as a function of locking depth, and a wide range of solutions have similarly low WRMS. Uncertainties are too large to warrant a full grid search (4 unknowns) for the 2-fault model. Compared to Lisowski et al. (1991), the multi-dislocation model for the San Andreas fault did not provide a better fit.

2-D elastic dislocation block modeling:

A more rigorous approach for estimating fault slip rates involves considering 2-D blocks bounded by different fault types of finite lengths because it accounts for changing fault geometry and allows strain partitioning, whereas the 1-D model assumes infinitely long strike-slip fault. The advantages of the 2-d model are: 1- allowing finite faults, 2- modeling strike slip faults in addition to thrust faults. Such 2-D models account for the spatial variations in the slip rate due to fault geometry and the effects of block rotations that are not considered in the 1-D model. The modeling approach used here follows the methodology of Meade and Hager (2005). The model allows no permanent deformation of the blocks or slip on unconnected faults. Strike slip faults are assumed vertical and the thrust fault belt is assigned with a 30° dip value. Faults were assigned the 15 km locking depth obtained in the 1-D double fault elastic dislocation model (15 km locking depth is consistent with dislocation models discussed previously). The strike slip faults in the locality of the LRB are well defined from historic earthquakes and geologic maps. On the other hand, the locality of the offshore thrust belt is not well mapped, but according to Elias et al. (2007) the thrust belt is limited to the south and the north by two oblique lateral faults: the Saida and the Rankine-Aabdeh faults (SF & RAF). The thrust belt is around 160 km in length and comes to a distance of 8 km away from the coast between Beirut and Enfe.
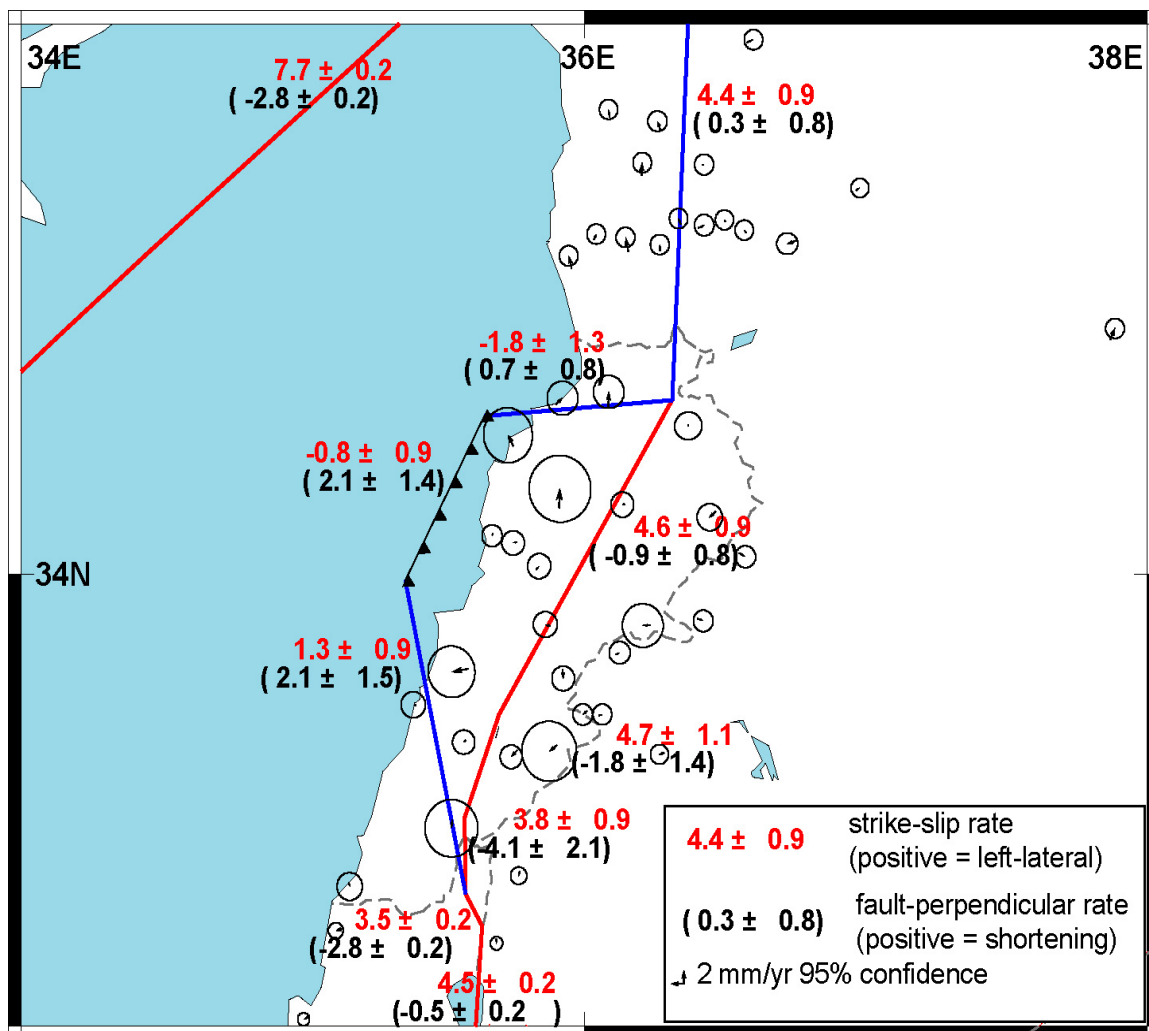
Figure 3.7: Map depicting elastic block model of a bend along a single fault trace. Red positive values indicate a sinistral sense of slip, while negative numbers indicate dextral sense of slip. Black positive values in parentheses indicated shortening and negative values designate an extensional scenario. Residuals of the velocities (mm/yr) to the best model and 1 sigma uncertainties are also shown.

Fault geometry shown in figure 3.7 includes a single strike-slip fault (YF) along the LRB because of the proximity of the YF and SF with respect to each other, and because the SF is unconnected (may terminate in Anti Lebanon). Block model was constrained with stations located all over the region in Sinai, Africa, Israel, Turkey, Cyprus, and Arabia. The residual fit of the optimal model is shown in figure 3.7 in addition to strike slip and fault normal displacement. Residual block motions for the Lebanese GPS sites excluding the second generation sites indicate very small values with minimal uncertainties meaning a good fit. Left-lateral slip rate of 4.6 ± 0.9 mm/yr was suggested by the block model for the LRB and this is consistent with the lower range of slip rates discussed earlier for the YF. Residuals along the southern DST segment suggest a good fit with a slip rate of 4.5 ± 0.2 mm/yr. On the other hand, residual block motions north of the bend in Syria show northward components, which indicate a poor fit. Residuals suggest a slower left-lateral rate on the northern DST segment than the 4.4 ± 0.9 mm/yr shown in figure 3.7. Since Sinai plate is also defined using sites with low uncertainties further to the south, good fits within the LRB and south of the bend associated with a poor fit north of the bend may indicate a separate block just north of the bend, and thus separating Sinai plate into two blocks separated at the northern edge of the LRB. Negligible components of shortening north of the bend and extension south of the bend are reported in this model.

The model also suggests a shortening rate of 2.1 ± 1.4 mm/yr accommodated by the offshore thrust belt. By considering the 1500 yr recurrence rate and the 80 cm uplift per event suggested by Elias et al., (2007) and assuming a 30° dipping thrust fault, ~140 cm of horizontal shortening per event was obtained from tangent trigonometric function.

Then, a 1.0 mm/yr geologic shortening rate was obtained by dividing the 140 cm horizontal shortening by the recurrence rate. The 1.0 mm/yr of geologic shortening lies within the lower range of the 2.1 ± 1.4 mm/yr suggested shortening.

2-D Continuum modeling (2-D velocity gradient modeling)

Whereas the dislocation models permit assessing fault slip-rates and locking depths for prescribed structures, the GPS velocities can also be used to assess other aspects of infinitesimal deformation, such as dilatations, rotations, and strains. This is accomplished by applying the algorithm of Allmendinger to calculate the velocity gradient field.

The Velocity gradient tensor (e_{ij}) is related to the GPS measured velocity (u_i) by:

$$u_i = t_i + e_{ij} \, x_j \qquad (3.2)$$

where t_i is a constant that represents the displacement at the origin of the system, and x_j being the station coordinate vector. A minimum of three stations are needed to determine the displacement gradient (rate). The equations are written in a matrix format and are solved with the standard weighted least squares solution of Menke (1984) when weighted by their distance to the point of computation.

The velocity gradient tensor for infinitesimal strains can be additively decomposed into an infinitesimal strain rate (ε_{ij}) and a rotation rate (ω_{ij}) as follows: $e_{ij} = \varepsilon_{ij} + \omega_{ij}$. Also, ε_{ij} and ω_{ij} are separated respectively into symmetric strain tensor and antisymmetric tensor. Instantaneous deformation (Infinitesimal strain and rotation rates) from GPS velocity vectors were calculated using the SSPX software (Cardozo & Allmendinger (SSPX v. 1.5)).

In the solution, a uniform grid is constructed for the area and the velocity gradients calculated at each node in the grid. Two approaches could be adopted in the modeling: the weighted and the nearest neighbor methods. The nearest neighbor method is based on specifying the number of nearest stations (neighbors) and the maximum distance away from each grid node for which stations are to be considered. In the distance weighted method, all stations in the network are used in the calculation but velocities from GPS stations are weighted with respect to their distance from the grid node with a function α, that specifies how the station effect would decay with distance from the grid node (Shen et al., 1996). The weighting factor is:

$$W = \exp(-d^2 / 2\alpha^2) \qquad\qquad (3.3)$$

where **d** indicates the distance between the node grid and the station. Stations located within 1 α distance contribute more than 67% to the solution, while stations located beyond 3 α distance would contribute to less than 1 % to our solution (Allmendinger et al. 2007).

<u>Infinitesimal strain:</u>

Horizontal infinitesimal strain rate is decomposed into two principal horizontal strain axes: shortening and extension axes. The maximum shear strain rate is a measure of overall magnitude of strain rate in a region and is oriented at 45° to the principal axes. In principle, the maximum shear strain should delineate locked fault zones, as long as the grid size is small enough to capture spatial variations in strain resulting from elastic strain accumulation. According to Savage and Burford (1973), 90% of locked fault strain accumulation is within 6.3 locking depths away from the fault. The 15 km locking depth obtained from the 1-D dislocation model, results in a zone of ~ 95 km of locked fault strain accumulation on either side of the fault.

Figure 3.8 shows the orientation of the shortening and the extension axes within the LRB striking NNW-SSE and ENE-WSW respectively. Whereas north and south of the bend they strike NW-SE and NE-SW. Maximum left lateral shear plane is shown in figure 3.9 to be identical in strike to the geometry of the bend within the vicinity of the bend. It changes from N-S north of the bend to NNE-SSW in present day Lebanon to return to the N-S eventually south of the bend. Maximum left lateral shear planes are more NE striking in the northern Anti-Lebanon and they strike farther east of the LRB. This reflects the Palmyride structural trend in Syria.

The orientation of shortening in the mid section of the bend is consistent with the one suggested by Ron (1987) in figure 1.6. Results are identical to what is expected within a restraining bend with respect to shortening and extension axes. The axes north and south of the bend mimic a strain ellipse of a left lateral strike-slip fault. The delineation of the strike of the LRB by the maximum left lateral shear plane indicates reliable and accurate GPS velocities and modeling.

Rotation rate:

Figure 3.8 indicates a clear but varying pattern of counter clockwise (CCW) rotation in the vicinity of the LRB. This CCW rotation rate is a combination: 1) of relative rotation of points located on both sides of the faults, 2) rotation due to changing fault geometry, and 3) rigid block rotations. The first component of rotation is caused by the differential left lateral sense of slip caused by the differential northward movement of Arabia and Sinai plates. The second component is rotation due to change in the fault geometry at the two ends of the bend. The third and last component is resulting from rigid block rotating about a vertical axis (book-shelf model), discussed in Chapter 1.

As shown in figure 3.9, the western side of the LRB (Sinai) undergoes a CCW rotation of $\sim 1.0^o$/MA north of the LRB, 0.45^o/MA at the northern part of the LRB, ~ 1.75-1.8^o/MA at the central-southern part of the LRB, and $\sim 1.1^o$/MA south of the bend. While the eastern side of the bend (Arabia) demonstrates $\sim 0.5^o$/MA north of the bend, $\sim 0.8^o$/MA at the northern part of the bend, $\sim 1.75^o$/MA at Mount Harmon, and $\sim 1.35^o$/MA south of the bend.

The above rotations do not reflect an anti-symmetric pattern of CCW rates that might be expected within a restraining bend. This may be caused by variations in fault patterns and geometries on either side of the bend (figure 1.1). Maximum rotation rates are observed in the central-southern section of the western LRB, and southern section of the eastern LRB. The western maximum rotation of ~ 1.75-1.8^o/MA is caused by an increase of CCW rigid block rotation resulting from higher GPS velocities in that part of the LRB and changing fault geometry at the exit of the LRB. Direction of rotation is consistent with paleomagnetic studies suggesting rigid block counterclockwise rotation (Ron, 1987) (Chapter1). The eastern maximum rotation of $\sim 1.75^o$ mm/MA is caused by a strike slip duplex bounding Mount Harmon between SF and RaF (Gomez et al. 2007). The Mount Harmon CCW rigid block rotation in Mount Harmon is documented by Ron (1987 & 1990). The decrease in rotations north of the LRB, on both sides of the bend, is consistent with the lower GPS velocities in that locality.

The exact age of these post-Cretaceous rotations is still uncertain (Gomez et al. 2007). By considering the 1°- 1.75^o/MA CCW rotation result shown in figure 3.8, a minimum duration of ~ 35 MA and a maximum duration of ~ 60 MA are required in order to complete the full 60° rotation suggested by Ron (1987).

Dilatation:

GPS does not provide reliable vertical velocities due to larger uncertainties in the vertical direction. As an alternative, one can evaluate the volume strain (dilatation) rate by assuming a constant volume (i.e; Poisson's ratio of ~ 0.5). When the sum of the shortening and extension rates is negative, this indicates excess shortening in the horizontal plane and requires vertical thickening to maintain constant volume. When the sum is positive, this indicates excess extension and requires vertical thinning in order to maintain a constant volume (Allmendinger et al. (2007).

The transpression zone generated by the restraining bend would suggest an excess compression and thus would be expected to be balanced by a thickening of the crust. This is consistent with Tiberghien (1974), who suggested regional eastward thickening of the crust within the LRB from gravity data. The generated 2-D dilatation model didn't show any significant dilatation, which is consistent with the absence of clear shortening or extension in figure 3.3 b. This could be caused by the fact that all uplift is accommodated by the offshore thrust belt, as suggested by the 2-D elastic block model, and that all the GPS sites are located east of the strike of the thrust belt on the hanging wall. Hence, if all GPS stations in the LRB are uplifting uniformly and measurements from the foot wall of the OTB are lacking, the 2-D dilatation calculation would not detect differential vertical movement within the LRB.
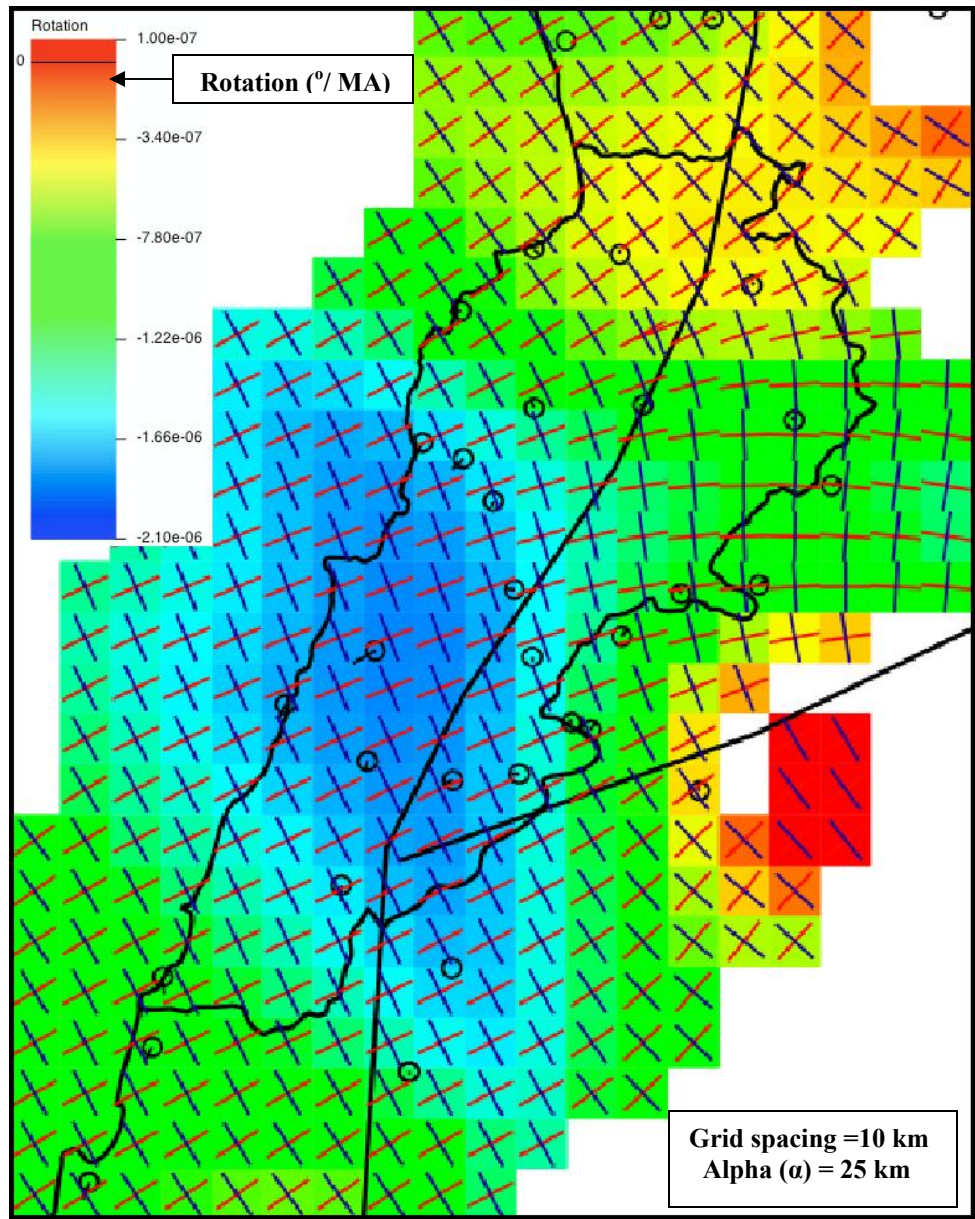
Figure 3.8: Map of GPS strain orientations and rotation rates for the LRB. Principal infinitesimal horizontal strain axes are shown with short colored lines segments: Red being the extension axes and blue being the shortening axes. Colored squares in this figure are an indication of the magnitude of rotation about a vertical, downward positive axis. Positive values indicate a clockwise sense of rotation, whereas negative values indicate a counter-clockwise sense of rotation.
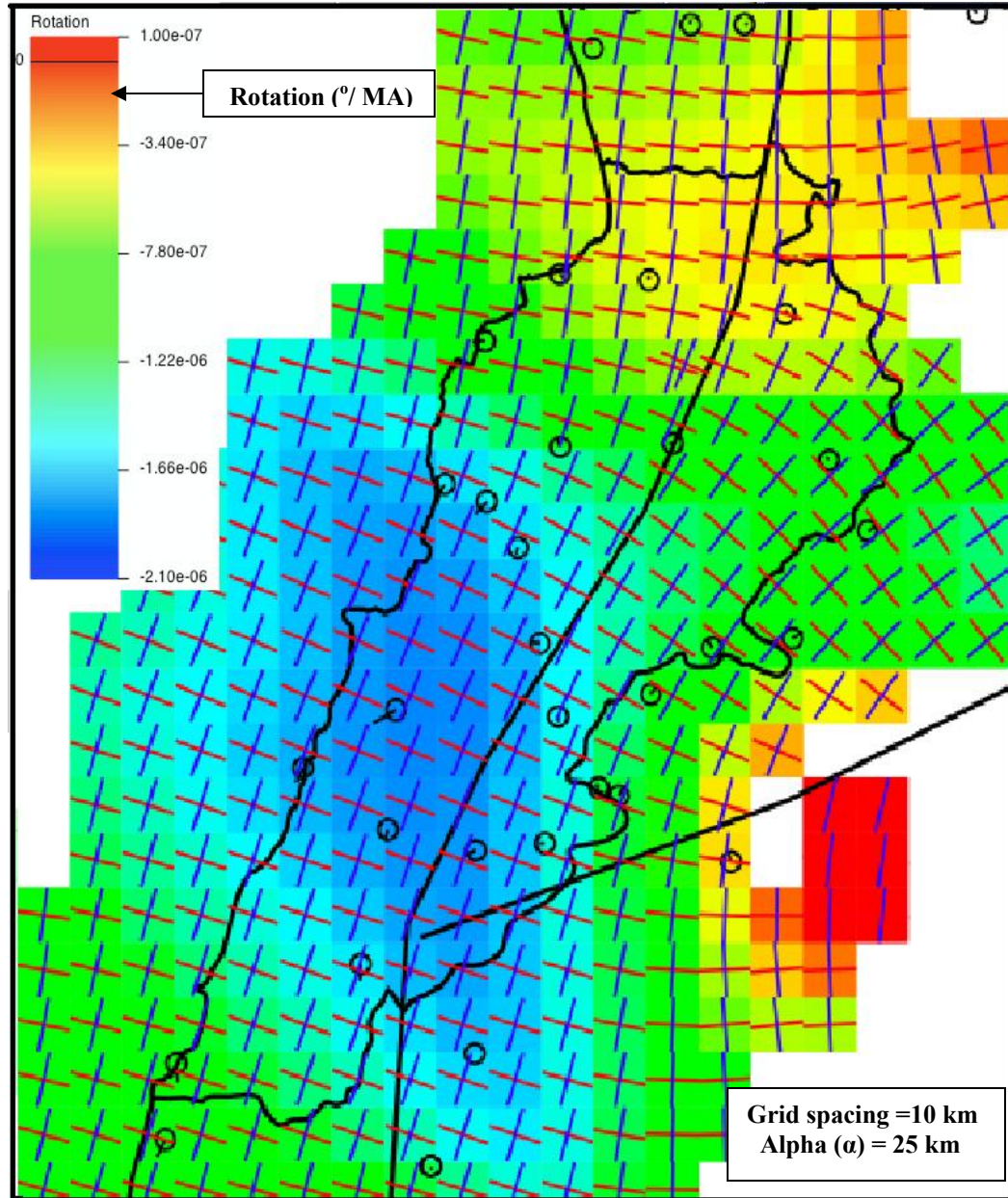
Figure 3.9: Map of the maximum left lateral shear strain orientation. The maximum left lateral axis orientation is indicated in blue and is delineating the locked fault zones (LRB).

Implications for Earthquake hazard:

Devastating historical seismic events (table 3.1) within present day Lebanon increase the urgency and importance of assessing earthquake hazard by considering maximum present-day prediction. This assessment is achieved with a deterministic seismic hazard approach.

Deterministic seismic hazard analysis:

This approach involves the development of a particular seismic scenario of earthquake hazard based on assessing the peak magnitude earthquake (moment magnitude) that could be produced in the present time by the YF and the offshore thrust belt. Moment magnitude relationship is defined as:

$$M_o = \mu * D_{av} * A \qquad\qquad (3.4)$$

$$M_w = 2/3 * \log M_o - 10.7 \qquad\qquad (3.5)$$

Where M_o is the seismic moment, μ is the modulus of rigidity of the crust, D_{av} is the average displacement on the fault during the earthquake, and A is the total area of rupture of the fault.

Rates of 5 mm/yr and 1 mm/yr were assigned for the YF and the offshore thrust belt (OTB). Dips of 90° and 30° were assigned for the YF and OTB with both assigned the 15 km obtained in the 1-D model (Consistent with D values adopted in previous dislocation models (Reilinger et al. 2006)), and spanning 160 km for the OTB (Elias et al., 2007) and 170 km for the YF (Chapter 1). Finally, D_{av} was calculated as the total slip elapsed since the last seismic event. Daeron et al., (2004) suggested from a paleoseismic study the May, 20, 1202 earthquake as the last event along the YF. While Elias et al., (2007) suggested the Jul 9, 551 earthquake as the last event along the offshore thrust belt.

Sources	Max Ms	References
Yammouneh fault	7.5	Ambraseys & Barazangi (1989)
Rachaya fault	6.6	Ambraseys & Barazangi (1989)
Serghaya fault	7.4	Ambraseys & Barazangi (1989)
Roum fault	7.1	Sbeinati et al. (2005)
Offshore thrust belt	7.2	Sbeinati et al. (2005)

Table 3.2: Representing the Maximum Earthquake magnitude (Ms) generated by faults within the LRB.

Peak moment magnitudes of 7.6 and 7.5 were obtained for the YF and OTB, respectively. Earthquakes of such magnitudes would be devastating for megacities like Beirut and Damascus that combine to a population of ~ 6 million. As for Lebanon, all Lebanese cities are located within a maximum distance of 50 km away from either faults, which puts the country as a whole under the mercy of a similar event (Table 3.1).

General tectonic implications:

Results discussed in this chapter indicate that the LRB is not a simple restraining bend. Slip rates decrease in the northern part of the bend (Figure 3.2). Total slip rate along the LRB is partitioned among the YF and SF unevenly, where the YF accommodates most of the total slip rate (Figure 3.6). Rotation rates within the LRB reveal a mirror CCW rotation pattern on the eastern and western sides of the bend, which is inconsistent with a typical restraining bend. Highest CCW rotation rates are located around the southern part of the bend and decrease gradually northward within the bend (Figure 3.8). Shortening across the bend is being accommodated by the offshore thrust belt (Figure 3.7). Sinai plate may be separated into two independent blocks at the northern part of the LRB by a fault transferring part of the strain away from the northern section of the DST.

Slip rates and rotation rates are expected to show a high covariance among them. This is in agreement with the decrease in slip and rotation rates observed in the northern part of the bend.

Figure 3.10 summarizes the above listed tectonic implications in a graphical manner. The rotation vectors represent the relative CCW in that specific locality. The scale of the arrows assigned to the YF and SF indicate sense and relative rate of slip.
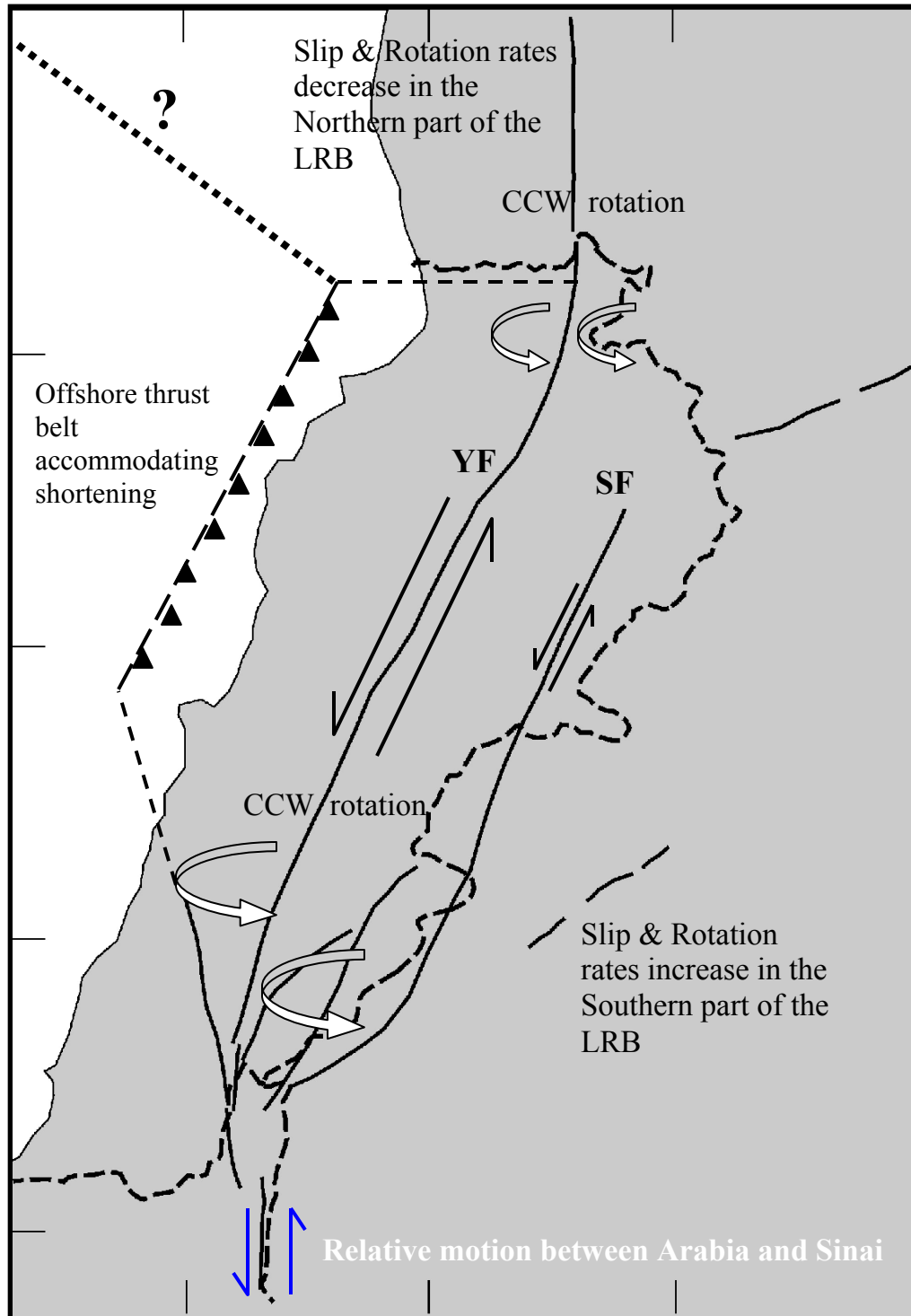
Figure 3.10: A cartoon of the general tectonic implications within the LRB. Different arrow size along the YF and SF are an indication of the amount of slip accommodated on each of them.

Conclusion:

   The GPS results presented in this study suggest geodetic measurements of the present day deformation within the LRB. To begin, The YF is presently accumulating strain, accommodating most of the expected strike slip motion of ~ 4.5 - 5.5 mm/yr, and is the main strand of the bend within present day Lebanon. Also, the northern part of the bend displays lower strain and is consistent with strain and rotation rates monitored in NW Syria. The SF is permissible with data and accommodates a small portion of total expected shear rate along the bend. When modeled along side with the YF, it permits more a realistic locking depth of 15 km. Furthermore, the shortening across the strike of the bend is to a large extent accommodated by the offshore thrust with a shortening rate of 2.1 ± 1.4 mm/yr. Moreover, the transpression zone is characterized by counter-clock wise sense of rotation that ranges from 1.75^{o}- 0.5^{o}/MA within the bend. Finally, Present day peak magnitude earthquakes generated by the YF and the OTB could be devastating and reach moment magnitudes of 7.6 and 7.5, respectively.

References

Allmendinger, W., Reilinger, R., Loveless, J., (2007), Strain and rotation rate from GPS in Tibet, Anatolia, and the Altiplano, *Tectonics,* 26, TC3013.

Altamimi, Z., Sillard, P., and Boucher, C., (2002), ITRF2000: A new release of the International Reference Frame for earth science applications, *Journal of geophysical research,* 107(B10), 2214.

Ambraseys, N.N. and Barazangi, M. 1989. The 1759 earthquake in the Bekaa valley: implications for earthquake hazard assessment in the eastern Mediterranean region. *Journal of Geophysical Research*, 94: 4007-4013.

Ambraseys N.N. and J.A. Jackson, 1997. Faulting associated with historical and recent earthquakes in the Eastern Mediterranean region.

Ambraseys, N.N., Melville, C.P. and Adams, R.D. 1994. The Seismicity of Egypt, Arabia and the Red Sea: a historical review. Cambridge University Press, 181p.

G. Blewitt. Basics of the GPS technique: Observation equations. *Geodetic Applications of GPS, Swedish Land Survey*, 1997.

Butler, R.W.H., Spencer, S., and Griffiths, H.M. 1998. The structural response to evolving plate kinematics during transpression: evolution of the Lebanese restraining bend of the Dead Sea transform. Edited by Holdsworth, R.E., Strachan, R.A. and Dewey, J.F. *Continental Transpressional and Transtentional Tectonics.* Geological Society, London, Special Publications, 135: 81-106.

Chaimov, T.A., Barazangi, M., Al-Saad, D., Sawaf, T., and Gebran, A. 1990. Crustal shortening in the Palmyride fold belt, Syria, and implications for movement along the Dead Sea fault system. *Tectonics*, 9: 1369-1386.

Daeron, M., Benedetti, L., Tapponnier, P., Sursock, A. and Finkel, R.C. 2004. Constraints on the post ~25-ka slip rate of the Yammouneh fault (Lebanon) using in situ cosmogenic Cl dating of offset limestone-clast fans. *Earth and Planetary Science Letters*, 227: 105-119.

Dubertret, L. 1940. Carte géologique au 1:50,000 feuille de Rachaiya-Nord avec notice explicative. République Libanaise, Ministère des travaux publics, 44p.

Dubertret, L. 1947. Problèmes de la geologie du Levant. *Bulletin de la Société Géologique de France,* (Serie 5), 17: 3-31.

Dubertret, L. 1951. Carte géologique au 1:50,000 feuille de Merdjayoun avec notice explicative. République Libanaise, Ministère des travaux publics, 64p.

Dubertret, L. 1955. Carte géologique du Liban au 1:200,000 avec notice explicative. République Libanaise, Ministère des travaux publics, 74p.

Dubertret, L. 1970. Review of structural geology of the Red Sea and surrounding areas. *Philosophical Transactions of the Royal Society of London,* 267: 9-20.

Elias, A., Tapponier, P., Singh, S.C., King, G.C.P., Briais, A., Daeron, M., Carton, H., Sursock, A., Jacques, E., Jomaa, R., and Klinger, Y. 2007. Active thrusting offshore Mount Lebanon: Source of the tsunamigenic A.D. 551 Beirut-Tripoli earthquake. *Geology*, 35: 755-758.

Fadil, A., 2006. Global positioning system (GPS) applications in and around Morocco.

Gomez, F., Meghraoui, M., Darkal, A.N., Hijazi, F., Mouty, M., Suleiman, Y., Sbeinati, R., Darawcheh, R., Al-Ghazzi, R., and Barazangi, M. 2003. Holocene faulting and earthquake recurrence along the Serghaya branch of the Dead Sea fault system in Syria and Lebanon. *Geophysical Journal International,* 153: 658-674.

Gomez, F. 2006. Global Positioning system measurements of strain accumulation and slip transfer through the restraining bend along the dead sea fault system in Lebanon. *Geophysical Journal International.*

Gomez, F., Karam, G., Khawlie, M., McClusky, S., Vernant, P., Reilinger, R., Jaafar, R., Tabet, C., Khair, K., and Barazangi, M., 2007. Global Positioning System measurements of strain accumulation and slip transfer through the restraining bend along the Dead Sea fault system in Lebanon, *Geophysical Journal International,* 168, 1021-1028.

Gregor, C.B., Mertzman, S., Nairn A.E.M. and Negendank J. 1974. Palaeomagnetism and the Alpine tectonics of Eurasia V: the paleomagnetism of some Mesozoic and Cenozoic volcanic rocks from the Lebanon. *Tectonophysics*, 21: 375-395.

Hancock, P.L. and Atiya, M.S. 1979. Tectonic significance of mesofracture systems associated with the Lebanese segment of the Dead Sea transform fault. *Journal of Structural Geology,* 1: 143-153.

Heimann, A. and Ron, H. 1987. Young faults in the Hula pull-apart basin, central Dead Sea transform. *Tectonophysics,* 141: 117-124.

Heimann, A., Eyal, M. and Eyal, Y. 1990. The evolution of Barahta rhomb-shaped graben, Mount Hermon, Dead Sea Transform. *Tectonophysics*, 180: 101-110.

Herring, T.A., King, R.W., and McClusky, S.C., 2006. Introduction to GAMIT/GLOBK. Release 10.2.

Herring, T.A., King, R.W. and McClusky, S.C., 1997. Geodetic constraints on interseismic, Coseismic, and postseismic deformation in southern California, *Annual Report to SCEC.*

Lisowski, M., Savage, J. C. & Prescott, W. H., 1991. The velocitiy field along the San Andreas fault in central and southern California. *J. geophys. Res.*, 96, 8369-8389.

Mahmoud, S., Reilinger, R., McClusky, S., Vernant, P., and Tealeb, A., (2005), GPS evidence for northward motion of the Sinai Block: Implications for E. Mediterranean tectonics, *Earth and Planetary Science Letters,* 238, 217-224.

Meade, B. J. & Hager, B., 2005. Block models of crustal motion in southern California constrained by GPS measurements. *J. geophys. Res.*, 110, doi: 10.1029/2004JB003209.

Menke, W., 1984, *Geophysical Data Analysis: Discrete Inverse Theory*, 260 p., Academic, Orlando, Fla.

Morhange, C., Pirazzoli, P.A., Marriner, N., Montaggioni, L.F., and Nammour, T. 2006. Late holocene relative sea-level changes in Lebanon, Eastern Mediterranean. *Marine Geology,* 230: 99-114.

Nemer, T., 2005. Sismotectonique et comportement sismique du relais transpressif de la faille de levant: roles et effets des brances de failles sur l'alea sismique du libans. PhD thesis, Universite Louis Pasteur, Strasbourg.

Nemer, T. and Meghraoui, M., 2006. Evidence of coseismic ruptures along the Roum fault (Lebanon): a possible source for the AD 1837 earthquake. *Journal of structural geology*, 28:1483-1495.

Pirazzoli P A, Bellevue M, Laborel J and Stiros S C 1996 Coastal indicators of rapid uplift and subsidence: examples from Crete and other eastern Mediterranean sites.

Reilinger, R., McClusky, S., Vernant, P., Lawrence, S., Ergintav, S., Cakmak, R., Kadirov, F., Guliev, I., Stepanyan, R., Mahmoud, S., Sakr, K., ArRajehi, A., Paradissis, D., Al-Aydrus, A., Evren, E., Dmitrotsa, A., Filikov, S. V., Gomez, F., Al-Ghazzi, R. & Karam, G., 2006. GPS Constraints on Continental Deformation in the Africa-Arabia-Eurasia Continental Collision Zone and Implications for the Dynamics of Plate Interactions. *J. geophys. Res.*, 111, doi:10.1029/2005JB004051.

Ron, H., Nur, A., and Eyal, Y. 1990. Multiple strike-slip fault sets: a case study from the Dead Sea transform. *Tectonics,* 9: 1421-1431.

Ron, H. 1987. Deformation along the Yammuneh, the restraining bend of the Dead Sea transform: paleomagnetic data and kinematic implications. *Tectonics,* 6: 653-666.

Sabbagh, G. 1962. Geological cross section across southern Lebanon. *American University of Beirut Archive*.

Sandvol, E. & Hearn, T., 1994. Bootstrapping shear-wave splitting errors. *Bulleting of the Seismological Society of America*, 84, 1971-1977.

Savage, J. C. & Burford, R. O., 1973. Geodetic determination of relative plate motion in central California. *J. geophys. Res.*, 78, 832-845.

Sbeinati, M.R., Darawcheh, R. and Mouty, M. 2005. The historical earthquakes of Syria: an analysis of large seismic events from 1365 B.C. to 1900 A.D. *Annals of Geophysics*, 48: 347-435.

Segall, P. and Davis, J. L., 1997. GPS applications for geodynamics and earthquake studies. *Earth Planet*. Sci. 1997. 25:301-36.

Shen, Z. k., D. D. Jackson, and B. X. Ge (1996), Crustal deformation across and beyond the Los Angeles basin from geodetic measurements, *J. Geophys. Res., 101,* 27,957-27,980.

Tiberghien, V., Le champ de la pesanteur au Liban at ses interpretations, *Pubs. Tech. Sci., 26, 193 pp.,* Ecole super.

Walley, C.D., 1998. Some outstanding issues in the geology of Lebanon and their importance in the tectonic evolution of the Levantine region. *Tectonophysics,* 298: 37-62.

Walley, C.D. 1988. A braided strike-slip model for the northern continuation of the Dead Sea fault and its implications for Levantine tectonics. *Tectonophysics,* 145: 63-72.